

UNCLASSIFIED

---

AD 260 819

*Reproduced  
by the*

ARMED SERVICES TECHNICAL INFORMATION AGENCY  
ARLINGTON HALL STATION  
ARLINGTON 12, VIRGINIA



---

UNCLASSIFIED

NOTICE: When government or other drawings, specifications or other data are used for any purpose other than in connection with a definitely related government procurement operation, the U. S. Government thereby incurs no responsibility, nor any obligation whatsoever; and the fact that the Government may have formulated, furnished, or in any way supplied the said drawings, specifications, or other data is not to be regarded by implication or otherwise as in any manner licensing the holder or any other person or corporation, or conveying any rights or permission to manufacture, use or sell any patented invention that may in any way be related thereto.

# DOFL *technical review*



## CONTENTS

NO. 5

JULY 1961

A 2D 30-Mc IF Amplifier George R. Yetter and Lawrence L. Hall . . .	1
Azimuthal Pattern of Slotted Array Antennas On a Cone Marie D. Prytulak . . . . .	17
Complementary Filtering R. N. Johnson and G. R. Hickox . . . . .	51
A New Electrochemical System for High-Voltage, Low-Current Drain Applications William J. Pauli . . . . .	67

CATALOGED BY ASTIA  
AS AD NO. \_\_\_\_\_

DIAMOND ORDNANCE FUZE LABORATORIES  
ORDNANCE CORPS • • DEPARTMENT OF THE ARMY  
WASHINGTON 25, D.C.

## FOREWORD

This, the fifth issue of the DOFL Technical Review, is composed entirely of new material which has not been published in any technical journal.

There are no fixed dates of issue; the publication will appear at such times as sufficient technical material has been collected to warrant issuance.

Published by the Diamond Ordnance Fuze Laboratories, Ordnance Corps, Department of the Army, Washington 25, D. C., for the purpose of disseminating technical information.

# A 2D 30-MC IF AMPLIFIER

by

George R. Yetter

Lawrence L. Hall

## ABSTRACT

A new concept in the design and packaging of microminiature high-frequency circuits has been developed at DOFL. With this concept, fixed-tuned, 30-Mc IF amplifiers with 100-db gain have been designed and built in volumes less than  $1/5$  in.<sup>3</sup>. An assembly consists of five stages, each built on a ceramic wafer measuring 0.6 x 0.6 x 0.020 in. Each stage has approximately 20-db gain at 30 Mc with a 6-Mc bandwidth. Five stages are inserted into separate compartments of partitioned brass holders, and printed wiring boards placed over the two open faces of the holders provide the interstage connections.

Electrically, each unit consists of five iterative, transformer-coupled amplifier stages with RC decoupling. The fixed-tuned toroidal transformers were trimmed to resonate with the total interstage capacitance. Amplifier stability was obtained by mismatching the stages. A noise figure of 8.5 db was obtained.

High-gain, rf linear circuits of this size have been nonexistent. The DOFL type of construction demonstrates a means by which circuits of this type can now be successfully built. The isolation of stages, the miniature toroidal transformers, and a shelved housing providing both shielding and rigidity are some of the design features that are successfully integrated in this model.

## 1. INTRODUCTION

Much exploratory work has been done with considerable success on miniaturizing digital circuitry. Digital circuitry is particularly adaptable to miniaturization both from circuit and economic viewpoints. In general, digital circuitry is built around resistances and capacitances (if core memories are disregarded) and is not too demanding of tight component tolerances. There is considerable duplication of circuits so

that the setup time and cost of the circuit preparation is amortized over many units. The frequency range is restricted.

Linear circuitry, in general, falls into another category. Circuit tolerances and stability requirements are usually tighter. There is less individual circuitry duplication for each piece of equipment. In addition, the unwelcome inductances present themselves all too often. There are many avenues of designing around tight tolerances and there exist techniques for resonant effects with RC-elements only. These concepts, however, each have distinct disadvantages.

The present work was initiated to explore the feasibility of micro-miniaturizing high-frequency linear circuitry. In particular, a high-gain 30-Mc IF amplifier strip was chosen as a vehicle. (A 30-Mc amplifier is a common commodity in ordnance electronic devices.) This selection provided the opportunity to explore shielding, coupling, and stray capacitances, and yet permitted the construction of an assembly using iterative stages. It is recognized that a lower intermediate-frequency amplifier would provide more formidable inductance problems while a higher-frequency amplifier would limit the number of available transistors.

The basic construction utilized the DOFL 2D technique. This technique uses silk-screened carbon resistors and silver conductors with ceramic capacitors constructed on and in a ceramic substrate. This type of construction is fairly well developed and can lead to more advanced metal-film types of construction where the stray capacitances and coupling problems are similar.

A volume of a fraction of 1 in.<sup>3</sup> was chosen, as an objective, preferably in cubical form for shock resistance and ease of packaging. This represents a two-order-of-magnitude size reduction from commercially available tube amplifiers of similar performance and more than one-order-of-magnitude reduction from transistor amplifiers.

## 2. DESIGN CONSIDERATIONS

### 2.1 Circuit Configuration

The choice of circuit design was based on the following requirements: (1) the circuit components should be adaptable to 2D techniques, (2) all stages should be identical for ease of fabrication, and (3) amplifier characteristics, such as automatic gain control, temperature

stability, and detection, should not be considered in the first model other than those qualities that could be obtained by sound design principles without the addition of extra components.

The circuit design (fig. 1) was patterned after the conventional transformer-coupled amplifier, with special emphasis on both decoupling networks and interconnections between stages, arranged so that potential ground loops would be minimized.

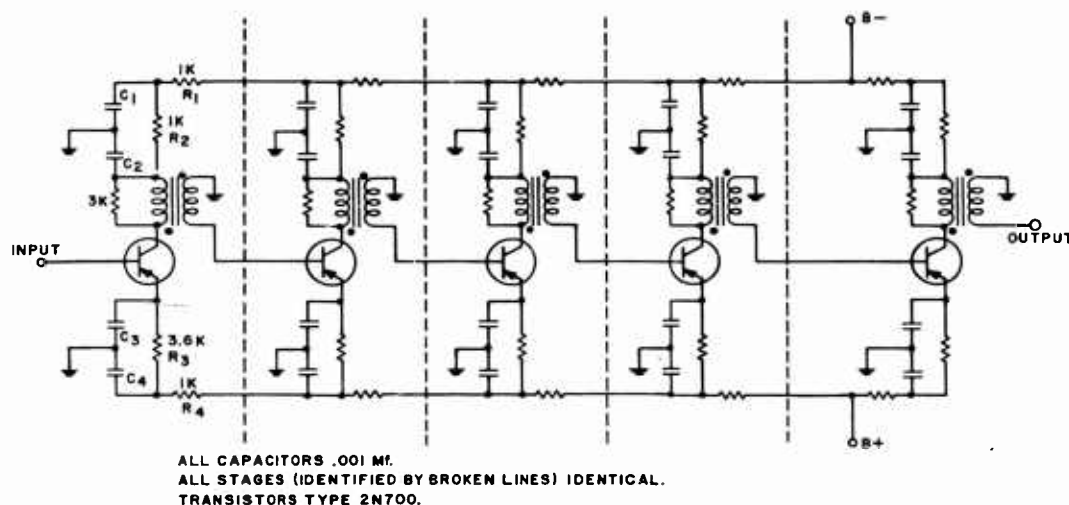


Figure 1. Circuit diagram of 30 Mc IF amplifier.

## 2.2 Transistor Selection

A search for commercially available transistors with at least 20-db gain at 30 Mc (ref 1) revealed that more than a dozen types were available. Several in this category were tried and performed satisfactorily at 30 Mc in a breadboard circuit. Of the transistors tried, type 2N700 was chosen for the following reasons:

- (1) The neutralized power gain of the transistor exceeds 25 db at 30 Mc.
- (2) The output capacitance of the transistor is low and closely controlled.

(3) The mechanical construction is such that it can be easily sliced to about 30 mils.

(4) The transistor is readily available.

### 2.3 Tuning

Transformer-coupled stages in conventional amplifiers are usually tunable. Since the state of the art has not as yet produced any suitable microminiature variable capacitors or inductors for use in this type of application, several other methods were considered. One of these methods utilized a paint that contained particles of the core material to tune the coil. Another method consisted in inserting a capacitor across the primary of the coil and then either scratching or filing the capacitor until the circuit resonated at the desired frequency. Both of these methods are cumbersome and primarily one-shot methods, since overpainting or overfiling result in overcompensation.

Fixed tuning was decided as a satisfactory compromise and the total interstage capacitance was used to tune the coil. From the manufacturer's data sheet (ref 2) the output capacitance of the transistor varied from 1.5 to 3.0 pf. The stray capacity on different parts of the ceramic plates was measured and the total stray capacity across the coil terminals estimated at 5 to 6 pf. A value of 7 to 8 pf was thus chosen as the total capacitance to tune the coil.

### 2.4 Transformer Design

A toroid was used for the transformer core, mainly because of low external field and flat construction. Using 7.0 pf for the total tuning capacitance, the inductance to resonate at 30 Mc was calculated to be 4.0  $\mu$ h. A maximum of 180 mils was set as the outside diameter of the transformer with a maximum thickness of 50 mils. Several cores were made from Teflon, polystyrene, and other nonmagnetic materials, but the self-resonant frequencies of the coils were too low for the size restrictions stated above and for the use of No. 40 wire. Different ferrites were tried and found to give good results. However, when the coils were duplicated, the results showed wide variations, found to be attributable to the heterogeneous nature of the core material. Toroids were then machined from standard iron tuning slugs (ref 3). Excellent results were obtained from these cores. Additional cores were machined, wound, and tested. The results showed little variation among transformers wound with the same number of turns.



The dimensions of the core are as follows: 0.175 in. o. d. by 0.015 in. thick, with a 0.046-in. drilled hole. Approximately 72 turns of No. 40 Formex wire gave the desired 4- $\mu$ h inductance.

The transistor parameters were measured to determine the input and output impedances so that the turns ratio of the transformer could be calculated. The parameters  $Y_{11}$  ( $=Y_{ie}$ ),  $Y_{21}$  ( $=Y_{fe}$ ), and  $Y_{22}$  ( $=Y_{oe}$ ) were measured successfully at 30 Mc. The measuring techniques did not provide an accurate measurement of  $Y_{12}$  ( $=Y_{re}$ ) at this frequency. For this reason  $Y_{ib}$  was measured so that  $Y_{re}$  might be calculated from the equation

$$Y_{re} = Y_{ib} - (Y_{fe} + Y_{oe} + Y_{ie})$$

This expression can be derived from the indefinite parameter matrix. Because  $Y_{re}$  is primarily determined by contributions from  $Y_{ib}$  and  $Y_{fe}$ , which are both large compared with  $Y_{re}$ , it can be seen that in taking the difference,  $Y_{ib} - Y_{fe}$ , a small error in either term will show up as a much larger error in  $Y_{re}$ . Additional experiments are contemplated to measure all the transistor parameters so that the transformer ratio and stage gain can be calculated for optimum values in the desired circuit.

From the manufacturer's data sheet (ref 2) the input and output impedances were estimated and by experimenting with different turns ratios, it was found that 8 to 1 gave the best results. The core and completed transformer are shown in figure 2.

Stability was achieved by mismatching the generator impedance (ref 4) rather than by capacity neutralization. A 3-kohm resistor, across the primary of the transformer accompanied by a loss of 6 db from the neutralized condition, stabilized the output when the stages were placed in series.

## 2.5 Decoupling Networks

Four stages of decoupling networks  $R_1C_1$ ,  $R_2C_2$ ,  $R_3C_3$ , and  $R_4C_4$  were used so that the power supply could be connected into the fourth and fifth stages in parallel and the other stages in series (fig. 1). This arrangement provides maximum voltage and current in the output stages for maximum dynamic range, and low voltage and current in the input stage for low noise.

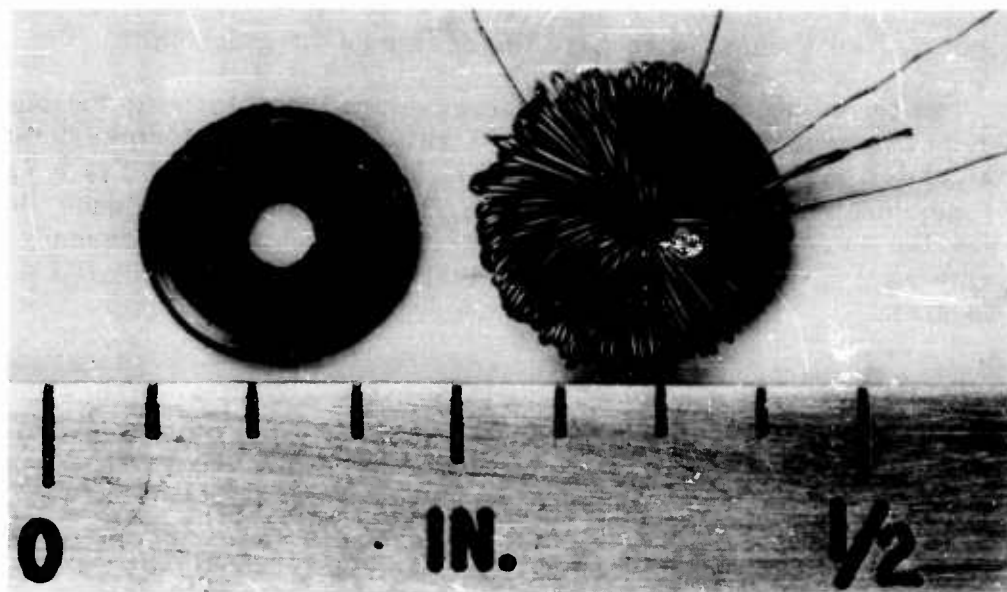


Figure 2. Interstage transformer.

### 3. FABRICATION

Ceramic plates 0.6 in. x 0.6 in. x 0.020 in. are used as the substrate. These plates, illustrated in figure 3, are fabricated in the manner described in reference 5. In brief, a 10-times scale layout is made, photographically reduced, and appropriate resistor and conductor screens are constructed. (ref 6). The conductive pattern is first screened on and fired. This is followed by an operation on an ultrasonic cutting tool in which all recesses are cut. The resistances are then screened on and cured at 250°C. The individual capacitors are cemented to a silver-sheet ground plane with a conductive adhesive. The subassembly is then cemented into the ceramic plate using unfilled epoxy resin. It can be seen that this silverbacked plate provides a low-resistance ground.

The coils are handwound and then trimmed on an RX meter to the proper value using the average of the measured distributed capacities as described above. This procedure produces transformers that fall within  $\pm 0.5$  Mc of the desired center frequency. The completed transformer is then cemented into the holes provided; the leads are attached to the transistor with conductive adhesive and to the output leads by soldering.

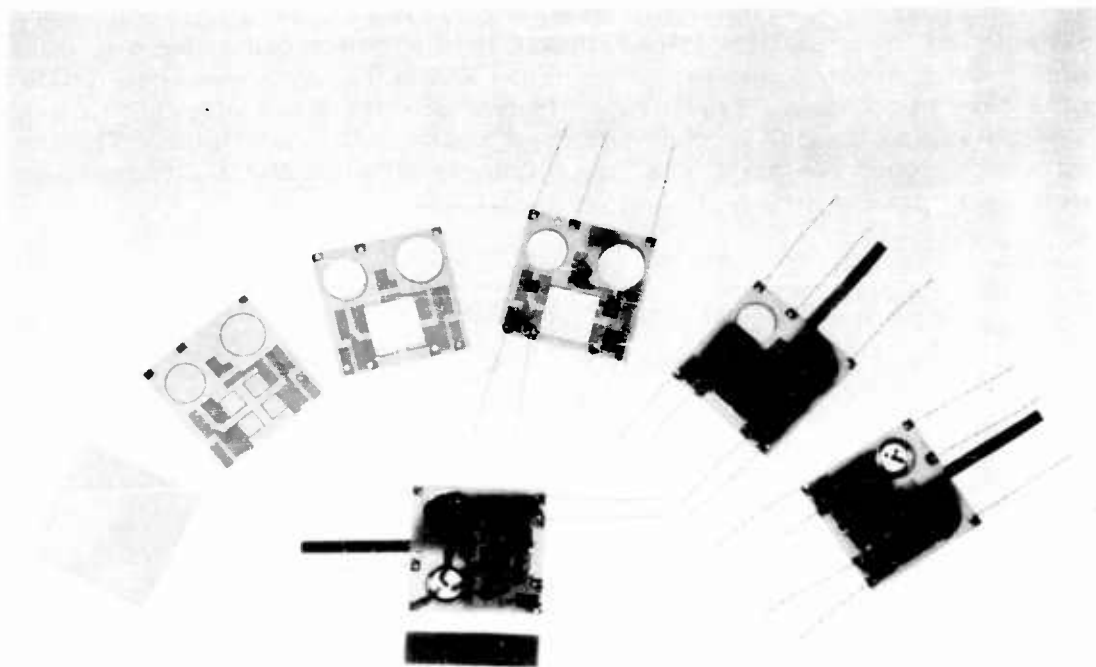


Figure 3. Steps in fabrication of an amplifier stage.

The transistor employed is a 2N700, modified as shown in figure 4. The objective of the modification is to reduce the height of the transistor. The end of the transistor is removed and the interior of the can is carefully cleaned. The can is then coated inside with KPR (Kodak Photo Resist) to protect the die from the deleterious effects of the subsequent epoxy potting. After potting, the transistor can be sliced to a thickness of about 0.030 in. Indexing the location of the cuts from a reference point on the header base permits this narrow slice to be accurately made. The slice contains both the transistor and the ends of the 0.017-in. header leads. These are wired into the circuit by the use of conductive adhesive.

The transistor in this form has only moderate resistance to environment, and it is anticipated that suitable hermetically sealed units will soon be available. It may be possible, however, to hermetically seal the complete IF-amplifier package.

The lead wires were initially solid wire fitted in grooves and fastened with conductive adhesive (fig. 5). This type of configuration presented a serious problem in reliability since the resin did not have sufficient

mechanical strength to withstand even normal breadboarding. Moreover, heat seemed to crystallize the resin and lead wires became loose in their joints. To overcome this problem, holes instead of grooves were drilled in the ceramic plates. Two strands of No. 38 wire were inserted through these holes and twisted to make a very strong mechanical joint. The loop that went through the plate was then soldered directly to the fired silver tab for a reliable electrical joint (fig. 6).

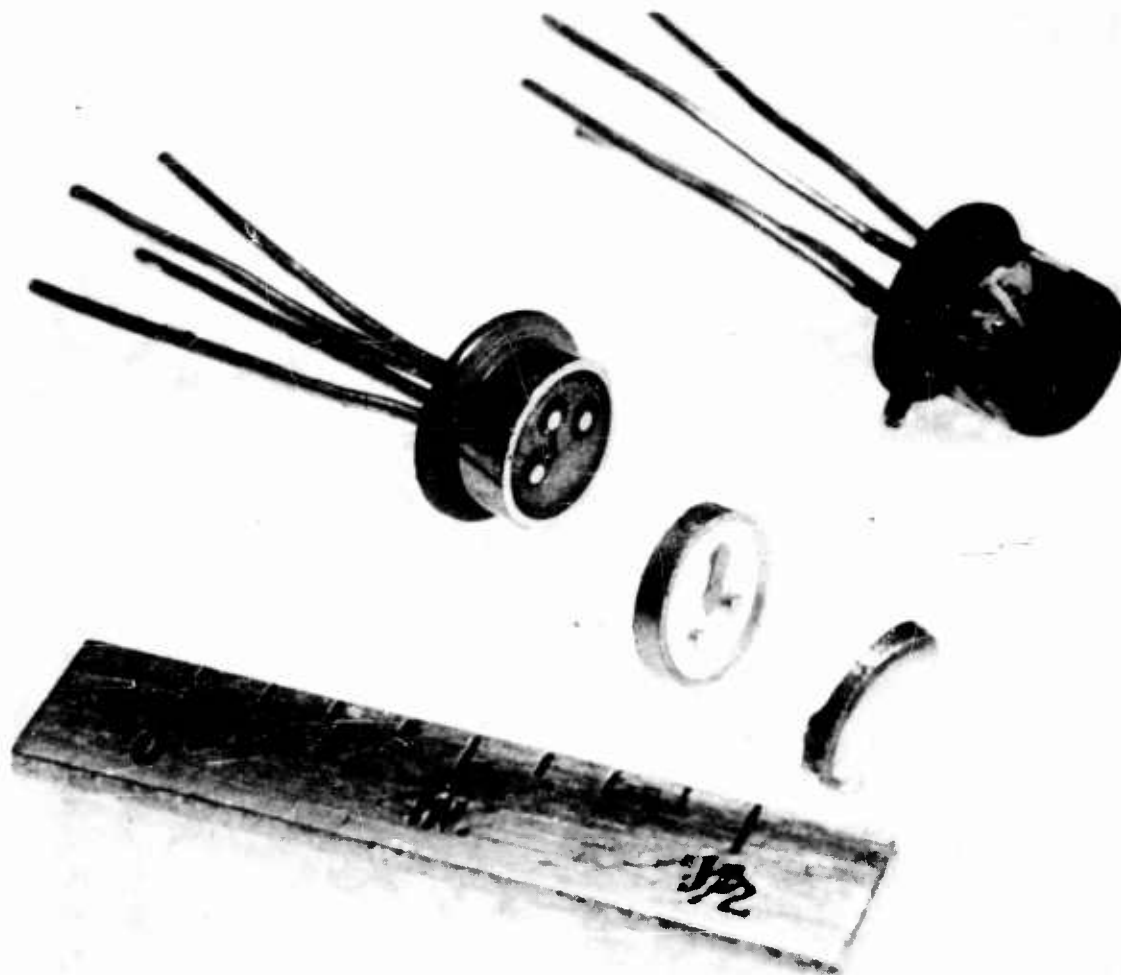


Figure 4. Transistor modification

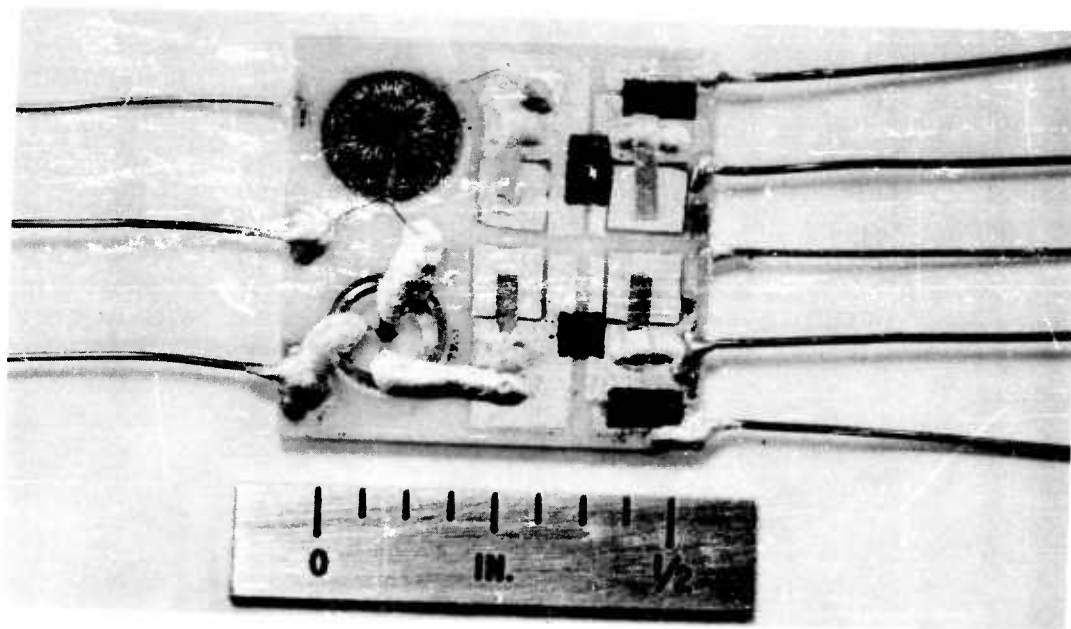


Figure 5. Initial amplifier stage.

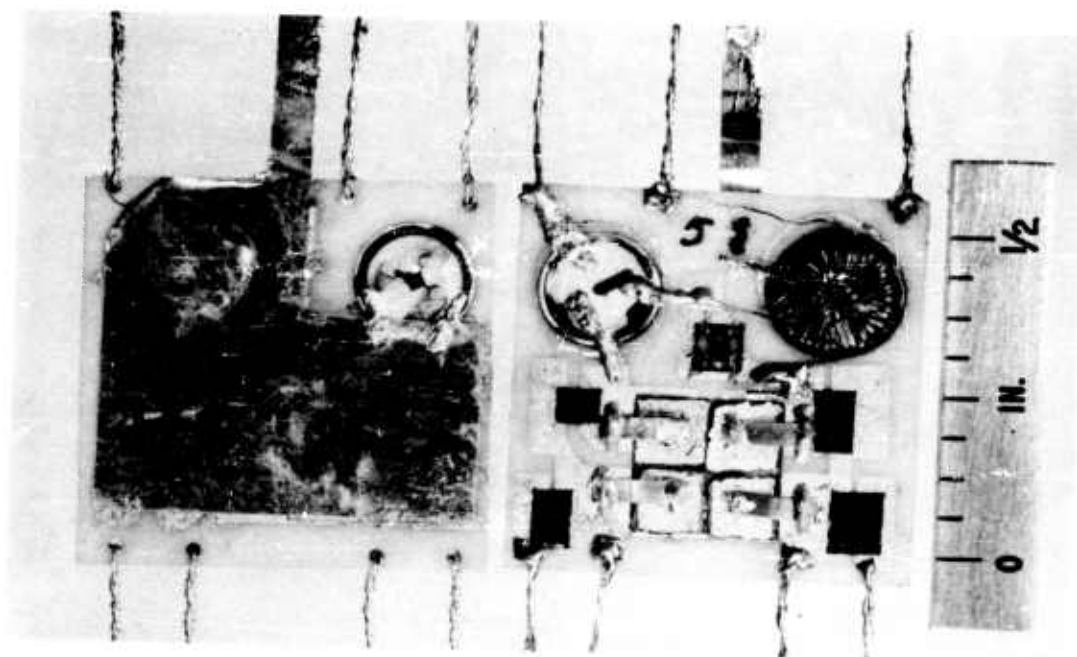


Figure 6. Amplifier stage of the present model.

#### 4. PACKAGING

Many types of packaging are possible and several were tried. Figure 7 shows an in-line type of construction in which the individual stages are constructed on separate plates and interconnected by a phenolic motherboard. The back side of the motherboard is copper-clad and provides a low resistance grounding surface. This type of construction permits measurements of circuit performance and might be called a 2D breadboard. All the stages may of course be constructed on one long ceramic board. At this stage of development, with frequent mechanical failures, individual circuit plates are highly desirable.

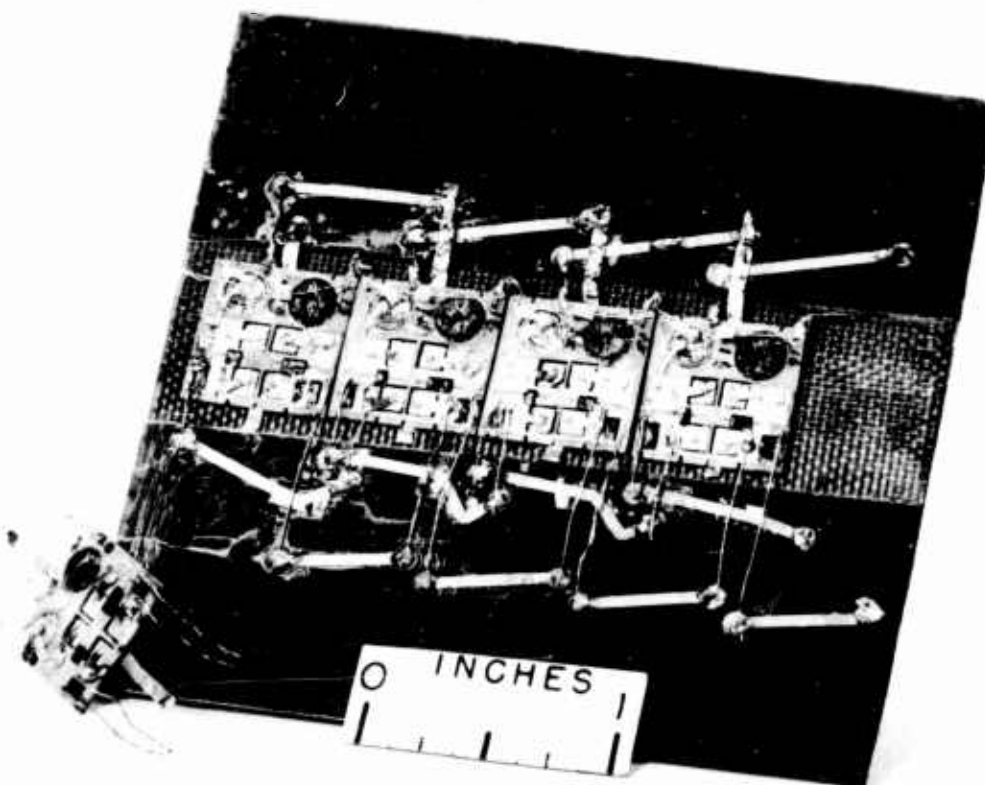


Figure 7. 2D breadboard of four-stage amplifier.

The problem of shielding was recognized early in the program. One attraction of the toroidal interstage transformers is their low external field. This fact coupled with the low impedances of transistor circuits in general indicated that shielding should not be a severe problem.

The first approach to a simple shielding technique is shown in figure 8. These stages were constructed as follows: The individual ceramic boards were constructed in a conventional manner and then potted in an epoxy resin in a very thin mold (0.060 in.). The potted assembly was then copper-plated by an electroless method, for interstage shielding. The advantage of this technique was that completely shielded individual stages (fig. 9) were then available for combining into an amplifier of any desired gain. There were, however, two serious objections to this method. The first was that the copperplating penetrated the surface imperfections, which were aggravated by the thin section, and produced many shorts. Visual inspection of the potted unit prior to plating usually did not reveal all these surface imperfections. A technique was developed to overcome this difficulty. The potted assembly was placed in a mild saline solution to which was added a small amount of phenolphthalein. All leads to the amplifier plate were connected together and placed in series with a battery and another electrode immersed in the solution. Any voids in contact with the solution would show an evolution of a red streamer whereby the voids could be located. This technique permitted the location (and patching) of imperfections before copperplating. Thus a few plated, operating stages were constructed and combined into an operating 60-db amplifier.

The second difficulty with this method was that the potted unit could not be reworked if failure occurred due to broken leads or transistor deterioration. Thus this technique was abandoned.

The present package makes use of the brass shelf-case arrangement shown in figure 10. The container has brazed shelves that provide the interstage shielding and the ground points for each stage. The walls of the case must be insulated and ordinary Mylar tape can be employed here. Experiments are being conducted so that the whole container can be immersed in an epoxy and then cured for a hard, insulating surface. The results of these experiments show promise as a production technique.

Printed-circuit boards are used for interconnecting the stages (fig. 10). Actually the wires are inserted through the holes in the board and soldered to a common point on the printed-wiring board halfway

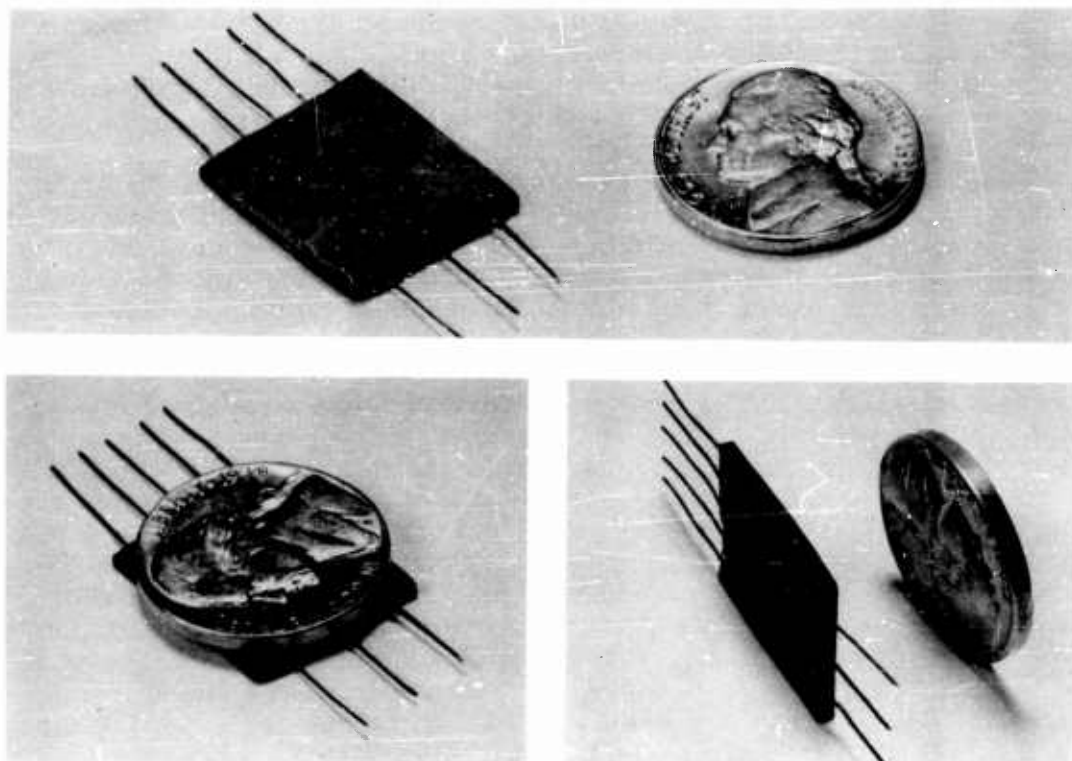


Figure 8. Shielding by copper cladding.

between the two holes, rather than at the holes themselves. In this way, the amplifier may be disassembled for repair.

## 5. ELECTRICAL CHARACTERISTICS

### 5.1 Summary of Typical Amplifier Operation Data

Gain	~100 db
Center Frequency	31.8 Mc
Bandwidth	30.3 - 32.6 Mc
Transistors	2N700 (modified)
V <sub>CC</sub>	-14 v at 6.5 ma
V <sub>EE</sub>	+14 v at 8.0 ma
Input termination	50 ohms
Output termination	50 ohms
Noise figure	8.5 db
Temperature range	-47°C to 73°C



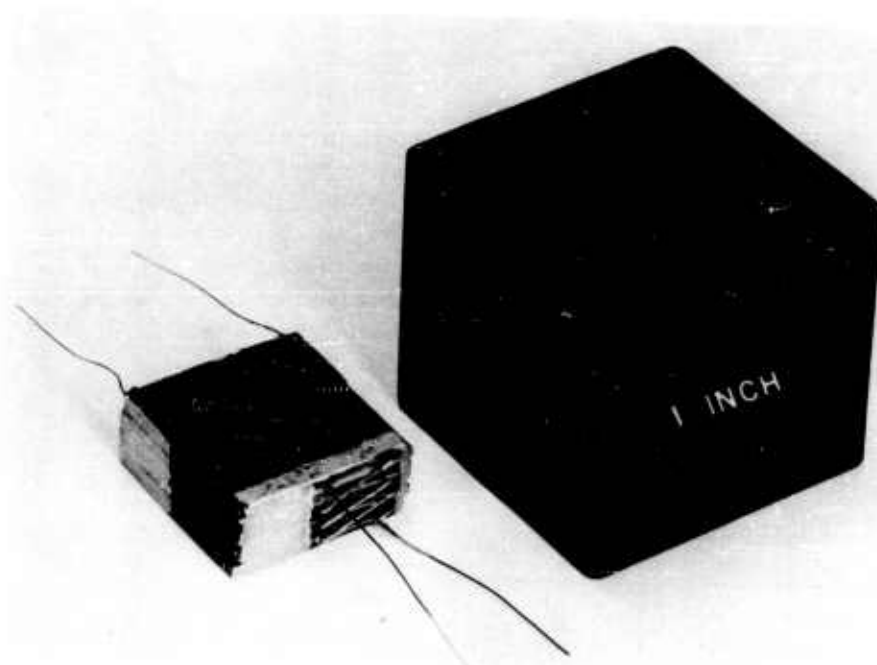


Figure 9. Proposed packaging of four-stage copperclad amplifier.

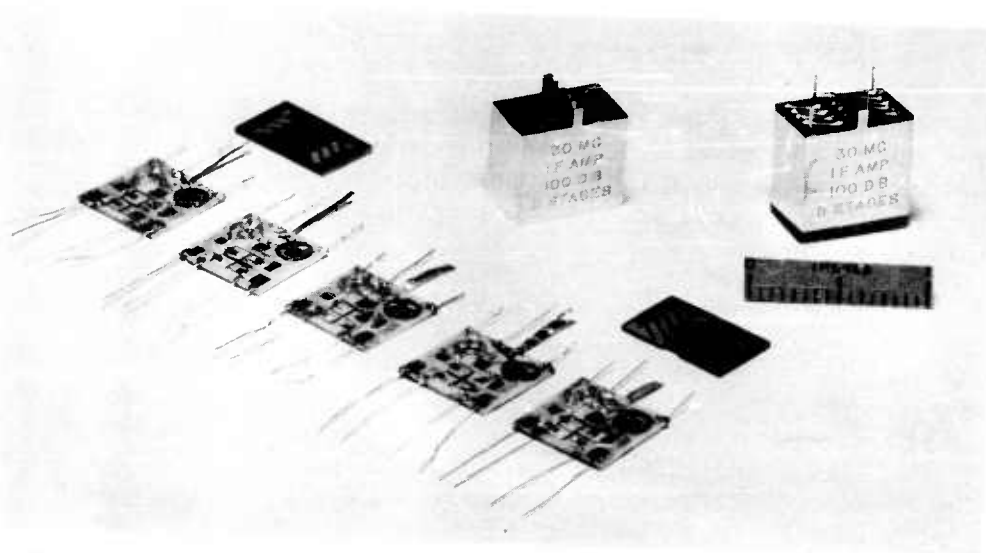


Figure 10. Elements and complete package of IF amplifier.

## 5.2 Discussion

### 5.2.1 Gain Measurement

The gain measurement was taken with the instruments diagrammed in figure 11. A signal generator was connected to the amplifier through a 50-ohm step attenuator. The output of the amplifier as measured on an rf voltmeter was adjusted to 250 mv by means of the signal generator. The rf voltmeter was then disconnected from the amplifier and attached directly to the attenuator. The attenuation was decreased until the meter read 250 mv as before. Thus the gain was read directly from the attenuator under matched conditions.

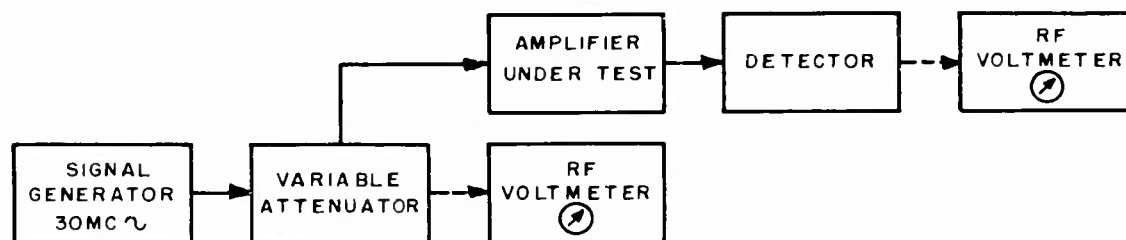


Figure 11. Instrumentation for gain measurement.

### 5.2.2 Noise Figure

The noise figure was measured on a HP Type-340A noise figure meter and found to be 8.5 db, with 50-ohm input termination. No attempt was made to improve this figure by the use of an input transformer. Also, it is not known at present if modifying the transistor degrades the noise figure.

### 5.2.3 Temperature Measurements

As mentioned previously, temperature compensation by the use of additional parts was not considered in this model. However, a preliminary temperature check was made and the results are shown in figure 12. No measurements were taken between room temperature (25°C) and -47°C. Observation of the output voltage in this range indicated no major deviations in the dotted portion of the curves of figure 12.

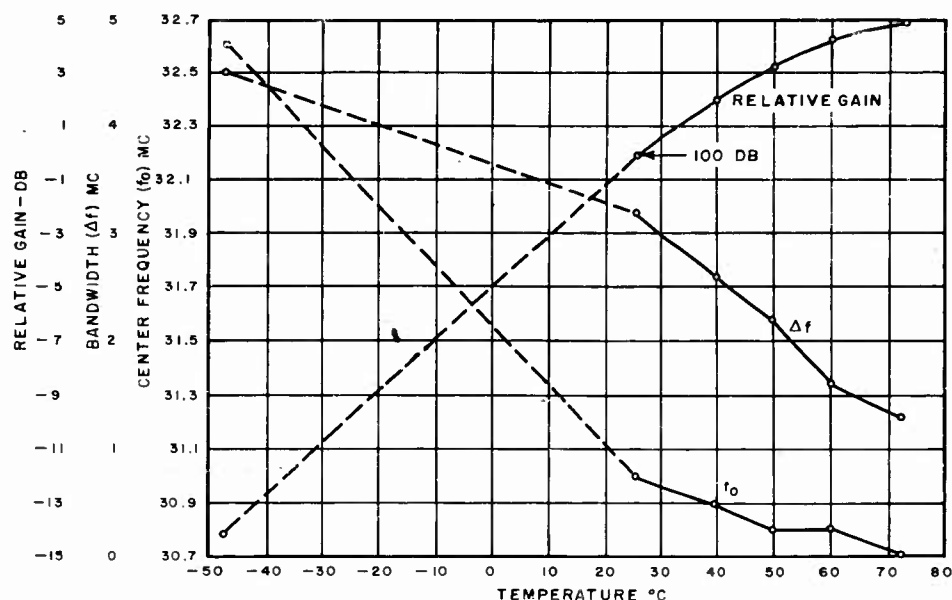


Figure 12. Temperature characteristics of amplifier.

## 6. SUGGESTIONS FOR FURTHER MINIATURIZING THE AMPLIFIER

No attempt was made in the first model to reduce further the size of the individual plates. As evident from the photographs, large areas of the substrate can still be eliminated. Additional work has been started to reduce the coil size by a factor of two. Lower-frequency, hermetically sealed, silicon transistors one-tenth the size of the germanium units now used are commercially available and it is hoped that comparable units suitable for this type of amplifier will be available in the near future. As soon as sufficient amplifiers are built, the decoupling network can be further analyzed and perhaps modified with a reduction of parts.

## 7. CONCLUSIONS

The feasibility of constructing microminiature 30-Mc IF amplifiers has been demonstrated. More than one hundred individual stages and three completed amplifiers have been built and tested to date. The techniques described are the results of many experiments that are not recorded in this report. The device described has certain deficiencies,

mainly lack of variable tuning and automatic gain control, and the uncertain shelflife of decayed transistors. For certain applications these restrictions are not prohibitive. Advancement in the art of microminiature variable capacitors and inductances, more elaborate circuitry, and suitable hermetically sealed transistors are possible remedies for these deficiencies. The packaging method is adaptable to other high-frequency applications.

#### 8. ACKNOWLEDGMENT

The authors are cognizant of the fact that valuable contributions by many DOFL personnel were instrumental in the final item and wish to acknowledge their help. In particular, Mr. David Williams, Br. 920 and Mr. John Cronin, Br. 210, for their technical assistance; Mr. Benjamin Mermelstein, Br. 920 for his circuit layout and fabrication techniques; Mr. Hayden Morris, Br. 920 for the potting and slicing of the transistor; Mrs. Mary Curtis; Mrs. Barbara Fairfield, Mrs. Della Stup, and Mrs. Virginia Stup, all of Br. 820 for their assistance in assembling the plates and to Mr. John Krawczyk, Br. 830 for his assistance in forming to size, the ceramic substrates by ultrasonic impact grinding.

#### REFERENCES

1. Datasearch Transistor Index - Datasearch Inc., Silver Spring, Md.
2. 2N700 Data Sheet, May 1, 1960, Motorola Semiconductors, Phoenix, Arizona.
3. Iron Tuning Slugs Part #20063-A, Cambridge Thermionic Corp., Cambridge, Massachusetts.
4. D. G. Paterson, "Circuit Design Considerations Using Mesa Transistors", Motorola Semiconductor Application Note No. 14, May 1, 1959.
5. T. A. Prugh, J. R. Nall and N. J. Doctor, "DOFL's Microelectronics Program", Proc. IRE, 47, n5, 882-894 (May 1959).
6. A. Smith, et al, DOFL Rept. No. R53-58-10, "Photographic Processes for Applying Patterns to Screens", 5 May 1958.

# AZIMUTHAL PATTERN OF SLOTTED ARRAY ANTENNAS ON A CONE

by

Marie D. Prytulak

## ABSTRACT

A theoretical approach for determining the azimuthal patterns for slotted array antennas on a cone is presented. Both one-way and two-way patterns are formulated for four equispaced antennas on a cone; a Tchebyscheff distribution is assumed in designing the antennas. Azimuthal patterns are calculated for antennas placed on cones having half-cone angles of  $5^{\circ}$ ,  $10^{\circ}$ , and  $15^{\circ}$ . These relative patterns are in agreement with experimental patterns, i.e., as the half-cone angle increases, the pattern takes on the appearance more and more of a clover leaf, since the nulls become deeper and wider at the angular positions where the antennas are located.

## 1. INTRODUCTION

Most of the knowledge of azimuthal patterns and azimuthal coverage for slotted array antennas placed on a conical surface has been obtained experimentally. For instance, the experimental patterns taken of four slotted array antennas on a cone indicate that the azimuthal patterns are a function of the half-cone angle of the apex of the cone. That is, as the half-cone angle is increased, the patterns appear more and more like that of a clover leaf since the nulls, which occur at the angular positions corresponding to the location of the antenna elements, become deeper and wider. Consequently, the azimuthal coverage has decreased as the half-cone angle has increased. Thus far little attempt has been made to theoretically confirm this picture.

Franklin Fletcher (ref 1), however, did derive the far-zone field intensity, from which the azimuthal patterns can be obtained, for four transmitting antennas mounted on a cone. In his analysis he assumed that the array factor for the principal plane pattern is a function of the half-power width and the half-angle of the conical pattern.

This report will confirm theoretically the experimental patterns for four slotted array antennas on a cone using Fletcher's analysis as a foundation, but his analysis will be modified and extended as follows. The

far-zone field intensity will be rederived with the assumption that the array factor is a function of a Tchebyscheff distribution, and both one-way and two-way azimuthal patterns will be considered.

For this analysis it will be assumed that there are four antennas mounted flush with the cone surface and equispaced around the circumference of the cone. Each of these antennas is a linear array of longitudinal slots cut in the broad face of a rectangular waveguide sustaining a  $TE_{10}$  mode. The slots are assumed to be resonant or very nearly so and are to be treated as isotropic point sources. In designing the antennas a Dolph-Tchebyscheff distribution is used (ref 2).

In slotted array antenna theory, use is made of the phenomenon of wave interference that occurs between the radiation from the different elements of the array. In the azimuthal and elevation patterns the nulls are due primarily to destructive wave interference. Therefore, one must consider such factors as phase differences between arrays, polarization, far-zone electric field intensity as a function of the elevation angle  $\theta$  and azimuthal angle  $\phi$ , etc.

## 2. FAR-ZONE ELECTRIC FIELD INTENSITY FOR ONE ANTENNA

Preliminary to obtaining the radiation pattern for a number of antennas on a cone, the far-zone field intensity  $\bar{E}$  for one slotted array antenna that is not on a cone is derived. This derivation is similar to the one in Fletcher's report (ref 1) but is modified as indicated in section 1.

It is assumed for each slotted array antenna that the slots, which are resonant (or very close to resonant), longitudinal, and cut in the broad face of a waveguide sustaining a  $TE_{10}$  mode, radiate as if cut in an infinite perfectly conducting plane surface. For such an array of slots the space radiation pattern is a figure of revolution about the axis of the array (it is really half a figure of revolution since only the radiation on one side of the plane is considered).

Although a single slot from such an array has a radiation pattern like that of a half-wave dipole, it will be assumed that the slot has a radiation pattern like that of an infinitesimal or a short dipole with electric and magnetic vectors interchanged. This approximation is allowable since the pattern or form factor of the infinitesimal or short dipole approximates closely the form factor of the half-wave dipole. The form factor of the short dipole is given by  $[\sin \theta]$  and of the half-wave dipole by

$[\cos(\frac{\pi}{2} \cos \theta) / \sin \theta]$ , where  $\theta$  is the elevation angle.

In addition, it is assumed that:

- the longitudinally slotted array antenna is placed along the z-axis and the slotted face is facing the positive x-direction (fig. 1); in the spherical coordinate system,  $\theta$  is the elevation angle and  $\phi$  is the azimuthal angle,
- as far as the far-zone is concerned, each of the individual slot patterns appears as though the radiation were coming from the origin,
- the principal plane of the antenna is the plane containing the axis of the antenna and perpendicular to the slotted face,
- there is an infinite flange on the slotted face (the flange is not shown on fig. 1).

Having assumed that a slot radiates as an infinitesimal or short dipole, the  $i^{\text{th}}$  slot produces a far-zone electric field given by, except for a proportionality constant,

$$\vec{E}_i = \hat{r}_i \times \vec{P}_i \left( \frac{e^{-jkr_i}}{r_i} \right) \quad (1)$$

where

$r_i$  = distance from slot to field point

$\hat{r}_i$  = unit vector pointing in that direction

$\vec{P}_i = \hat{i}_z P_i$  = complex vector strength of the slot (ref 1)

$\hat{i}_z$  = unit vector in positive z-direction

$k$  = propagation constant.

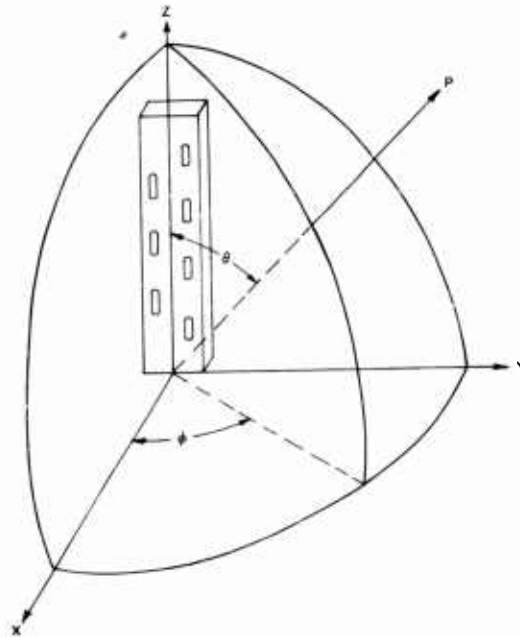


Figure 1. Antenna and coordinates

The total field  $\vec{E}$  due to  $n$  slots in the array is then given by

$$\vec{E} = \sum_{i=1}^n \hat{r}_i \times \hat{i}_z P_i \left( \frac{e^{-jkr_i}}{r_i} \right) \quad (2)$$

Since only the distant radiation fields are required, the following far-zone approximations can be made:

- Let  $\hat{r}_i$  be approximated by  $\hat{R}$ , where  $\hat{R}$  is the unit radial vector.
- For the inverse-distance factor  $r_i$  in the denominator, let  $r_i$  be approximated by  $R$ , where  $R$  is the distance from the origin.
- In the phase factor  $e^{-jkr_i}$ , it is the difference between  $r_i$  and  $R$  that is important. For very large values of  $r_i$  the lines to the point  $P$  are essentially parallel and the approximation for  $r_i$  can be written as

$$r_i = R - s_i \cos \theta$$

where  $s_i = z$ -coordinate of the  $i^{\text{th}}$  slot.

When the preceding approximations are made, equation (2) becomes

$$\vec{E} = \sum_{i=1}^n \hat{R} \times \hat{i}_z P_i \left( \frac{e^{-jk(R-s_i \cos \theta)}}{R} \right) \quad (3)$$

Equation (3) may be rewritten as

$$\vec{E} = \hat{\phi} \frac{e^{-jkR}}{R} \sin \theta \sum_{i=1}^n P_i e^{jks_i \cos \theta} \quad (4)$$

where  $\hat{\phi}$  is a unit vector pointing in the direction of increasing azimuthal angle  $\phi$ . The quantity

$$\left\{ \sin \theta \sum_{i=1}^n P_i e^{jks_i \cos \theta} \right\}$$



is the form factor of the array. Note that the form factor is independent of the variable  $\phi$ , thus implying that the space pattern is a figure of revolution about the  $z$ -axis. To compute the pattern in any elevation plane, it is sufficient to know the pattern in the principal plane.

In order to study the azimuthal characteristics that pertain to the major lobe alone, a principal plane pattern will be assumed. Since a Dolph-Tchebyscheff optimum distribution is used in designing the antenna, it is desirable to choose the Tchebyscheff polynomial to be the array factor of the principal plane pattern since the side-lobes will then be included. A property of the Tchebyscheff polynomial is that if the side-lobe level is specified then the beamwidth is minimized, but if the beamwidth is specified then the side-lobe level is minimized.

The Tchebyscheff polynomial may be designated in general by

$$T_m(z) = \cos \left( m \frac{\psi}{2} \right) \quad (5)$$

where  $m$ , with respect to the array, is one less than the total number of radiators. The variable  $z$  is restricted to the range  $-1 \leq z \leq +1$  and is given by

$$z = \cos \frac{\psi}{2} \quad (6)$$

$\psi$  is the phase difference and is given by

$$\psi = \beta d \cos \theta + \delta \quad (7)$$

where

$d$  = distance between isotropic point sources

$\beta d = 2\pi d/\lambda$  = the distance between sources in radians

$\lambda$  = free-space wavelength

$\delta$  = progressive phase shift between elements

$\theta = \theta_b$  = the angles (with respect to the array axis) at which maxima occur when  $\psi = \pm 2b\pi$  ( $b = 0, 1, 2, \dots$ ) and  $b$  indicates the spectrum order.

In designing a slotted array antenna it is desired to have in the elevation pattern only one major lobe with all other lobes greatly suppressed or eliminated. Almost all antennas are designed for either the zero-order lobe ( $b = 0$ ) or the first-order lobe ( $b = 1$ ). The angles of these major lobes can be found from

$$\cos \theta_0 = \lambda / \lambda_g \quad (8)$$

$$\cos \theta_1 = \lambda / \lambda_g - \lambda / 2d \quad \text{for staggered slots} \quad (9a)$$

$$\cos \theta_1 = \lambda / \lambda_g - \lambda / d \quad \text{for nonstaggered slots} \quad (9b)$$

In the subsequent pages, only for lobes other than first-order lobes will the angle  $\theta$  have subscripts; that is, as long as it is a first-order lobe no subscript will appear with  $\theta$ .

- For longitudinal slots, treated as point sources and cut in the broad face of a rectangular waveguide sustaining a  $TE_{10}$  mode, the phase lag or phase shift  $\delta$  is given by

$$\delta = - 2\pi d / \lambda_g \quad (10)$$

where  $\lambda_g$  is the waveguide wavelength.

Using equations (7), (8), and (10), one obtains for equation (6)

$$z = \cos \left[ \frac{\pi d}{\lambda} (\cos \theta - \cos \theta_0) \right] \quad (11)$$

which is applicable for nonstaggered slots. For staggered slots equation (11) is written as

$$z = \cos \left[ \frac{\pi d}{\lambda} (\cos \theta - \cos \theta_0) + \frac{\pi}{2} \right] \quad (12)$$

To introduce the side lobes, let the desired ratio of main-lobe maximum to minor-lobe level be  $R'$ , that is

$$R' = \frac{\text{main-lobe maximum}}{\text{side-lobe level}} \quad (13)$$

If the Tchebyscheff polynomial of order  $m$  is represented by  $T_m(z) = \cos(m\psi/2)$ , then the value of the polynomial at the center of the major lobe is  $T_m(z_0) = R'$ . The polynomials can be expressed over the whole pattern range by the pair of relations

$$T_m(z z_0) = \cos (m \cos^{-1} z z_0) \quad z z_0 \leq 1 \quad (14)$$

$$T_m(z z_0) = \cosh (m \cosh^{-1} z z_0) \quad z z_0 > 1$$

where  $z_0$  is a scale factor used to maintain the restricted range of -1 to +1.  $z$  is given by equations (11) and (12) and  $z_0$  is given by

$$z_0 = \cosh \left( \frac{1}{m} \cosh^{-1} R' \right). \quad (15)$$

By properly choosing the reference for the phases of the  $P_i$ 's, the form factor in equation (4) may be set equal to the form factor of the principal plane pattern given by equation (14), thus

$$\sin \theta \sum_{i=1}^n P_i e^{j k s_i \cos \theta} = \cos (m \cos^{-1} z z_0) e^{j \phi} \quad (16)$$

where  $\phi$  is a phase constant.

Now let  $\cos \theta = u$ .

$$\sum_{i=1}^n P_i e^{j k s_i u} = \left[ \frac{\cos (m \cos^{-1} z z_0)}{\sqrt{1 - u^2}} \right] e^{j \phi} \quad (17)$$

where  $z_0$  is given by equation (15) and  $z$  is given by equations (11) and (12) with the proper substitution, that is

$$z = \cos \left[ \frac{\pi d}{\lambda} (u - \cos \theta_0) \right] \quad \text{for nonstaggered slots and}$$

$$z = \cos \left[ \frac{\pi d}{\lambda} (u - \cos \theta_0) + \frac{\pi}{2} \right] \quad \text{for staggered slots.}$$

Now equation (17) may be written

$$\sum_{i=1}^n P_i e^{jks_i u} = f(u) e^{j\sigma} \quad (18)$$

where the function  $f(u)$  is defined by

$$f(u) = \frac{\cos(m \cos^{-1} u)}{\sqrt{1-u^2}} \quad (19)$$

In terms of the function  $f(u)$ , equation (4) may now be written

$$\vec{E} = \hat{\phi} \left( \frac{e^{-jkR}}{R} \right) \sin \theta f(u) e^{j\sigma} \quad (20)$$

The azimuthal characteristics for one antenna can now be determined from the preceding far-zone field intensity formulation.

### 3. A ONE-WAY AND A TWO-WAY PATTERN

At this point it is necessary to define the terms of a one-way and a two-way pattern. First it is to be noticed that the field intensity  $\vec{E}$  just derived was for a transmitting antenna. However, the formulation is equally valid for a receiving antenna since the reciprocity theorem holds; that is, the impedance and the pattern are the same for both a receiving and a transmitting antenna.

The radiation pattern of either a receiving or a transmitting antenna defines a one-way pattern. A one-way pattern is not necessarily limited to a pattern of just one transmitting (or receiving) antenna; the pattern may be the result of one or more transmitting (or receiving) antennas.

A two-way pattern (ref 3) results from a combination of a transmitting and a receiving antenna, that is, it is a transmitter-to target-to receiver radiation pattern. Here one antenna may act both as a transmitting and as a receiving antenna; or there may be a pair of antennas, one specifically for transmitting and the other for receiving. The number of the transmitting-receiving combination is not limited to one.

If a two-way pattern recorder (ref 3) is not available, the two-way pattern may be obtained by multiplying the pattern of the transmitting antenna by the pattern of the receiving antenna or for identical transmitting and receiving antennas, using the reciprocity theorem, the two-way pattern may be obtained by squaring the pattern of either.

#### 4. SLOTTED ARRAY ANTENNAS ON A CONE

Thus far, one-way and two-way patterns have been defined and the far-zone field intensity for one antenna on a plane surface has been derived. Now, with this as background, the far-zone field intensity for slotted array antennas mounted on a cone will be formulated. The azimuthal characteristics will be obtained from the far-zone field intensity in the form of the one-way and two-way patterns.

Of primary interest here is the azimuthal pattern through the main lobe for four slotted array antennas equispaced around the circumference of a cone. These antennas are designed to have broadside or near-broadside patterns with respect to the cone axis. It is assumed that the azimuthal coverage of each antenna is less than  $180^\circ$ . Under these conditions only two antennas need be considered, since only one pair can contribute radiation to the main lobe at any orientation with just one exception: When the target horn is looking directly at one antenna, radiation may be received equally from each adjacent antenna. It is assumed that the azimuthal coverage of each antenna is sufficiently less than  $180^\circ$  so that this effect can be neglected. Thus, the radiation pattern for four antennas can be obtained by considering one pair only.

#### 5. FAR-ZONE FIELD INTENSITY FOR FOUR SLOTTED ARRAY ANTENNAS EQUISPACED ON A CONE

As explained in the preceding section, the formulation of the far-zone field intensity for four slotted array antennas equispaced on a cone will be limited by geometry to two antennas. The one-way and the two-way patterns, and thus the azimuthal characteristics, will be obtained from the far-zone field intensity for this geometry.

All previous assumptions made will be maintained. At first the antennas will be treated as transmitting antennas and the one-way pattern obtained. Then proper adjustments will be made to obtain the two-way patterns where in one case one antenna is transmitting and one is receiving, and in the other case where there are two transmitting-receiving antennas.

The two antennas are placed on the cone (fig. 2) where the slotted face of antenna one is facing in the positive y-direction, the slotted face of antenna two is facing in the positive x-direction,  $a$  is the radius at the base of the cone,  $s_i$  is the distance of the  $i^{\text{th}}$  slot from the end of the antenna nearest the base of the cone, and  $\alpha$  is the half-angle of the cone.

At a point P in space the field  $\vec{E}$  of the two antennas, having positive x and y coordinates, is given by

$$\vec{E} = \sum_{i=1}^n \hat{r}_{i1} \times \vec{P}_{i1} \left( \frac{e^{-jkr_{i1}}}{r_{i1}} \right) + \sum_{i=1}^n \hat{r}_{i2} \times \vec{P}_{i2} \left( \frac{e^{-jkr_{i2}}}{r_{i2}} \right) \quad (21)$$

Since the antennas are alike, the vector strengths  $\vec{P}_{i1}$  and  $\vec{P}_{i2}$  are given by

$$\begin{aligned} \vec{P}_{i1} &= (0, -\sin \alpha, \cos \alpha) P_i \\ \vec{P}_{i2} &= (-\sin \alpha, 0, \cos \alpha) P_i \end{aligned} \quad (22)$$

where the terms of the parentheses are the components of the unit vectors  $(\hat{i}_x, \hat{i}_y, \hat{i}_z)$  pointing in the directions of increasing distance  $s$  along the two antennas.

The following far-zone approximations will be made:

- a)  $\hat{r}_{i1}$  and  $\hat{r}_{i2}$  are approximated by  $\hat{R}$  where  $\hat{R}$  is the unit radial and its components are given by

$$\hat{R} = (\sin \theta \cos \phi, \sin \theta \sin \phi, \cos \theta) \quad (23)$$

- b)  $r_{i1}$  and  $r_{i2}$  in the denominator are approximated by  $R$  in amplitudes.

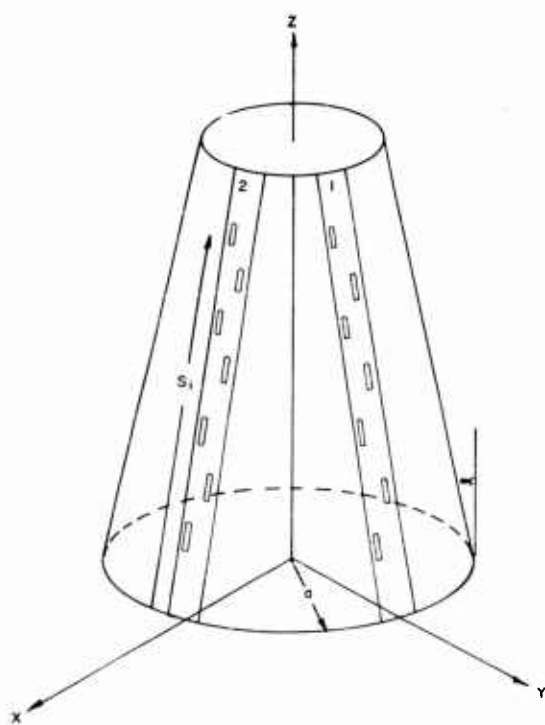


Figure 2. Two of the four antennas on a cone

c)  $r_{i1}$  and  $r_{i2}$  in the phase factors  $e^{-jkr_{i1}}$  and  $e^{-jkr_{i2}}$  are approximated by

$$\begin{aligned} r_{i1} &= R - \vec{R} \cdot \vec{\rho}_{i1} \\ r_{i2} &= R - \vec{R} \cdot \vec{\rho}_{i2} \end{aligned} \quad (24)$$

where  $\vec{\rho}_{i1}$  and  $\vec{\rho}_{i2}$  are position vectors of the  $i^{\text{th}}$  slots on the respective antennas with components

$$\begin{aligned} \vec{\rho}_{i1} &= (0, a - s_i \sin \alpha, s_i \cos \alpha) \\ \vec{\rho}_{i2} &= (a - s_i \sin \alpha, 0, s_i \cos \alpha) \end{aligned} \quad (25)$$

Using equation (22) and the far-zone approximations in equation (21), then suppressing  $(e^{-jkR}/R)$  and performing the vectorial operations, one obtains for equation (21)

$$\begin{aligned} \vec{E} &= \sum_{i=1}^n (u_1, -\sin \theta \cos \phi \cos \alpha, -\sin \theta \cos \phi \sin \alpha) P_i e^{jk(a \sin \theta \sin \phi + s_i u_2)} \\ &+ \sum_{i=1}^n (\sin \theta \sin \phi \cos \alpha, -u_3, \sin \theta \sin \phi \sin \alpha) P_i e^{jk(a \sin \theta \cos \phi + s_i u_4)} \end{aligned} \quad (26)$$

where

$$\begin{aligned} u_1 &= \sin \theta \sin \phi \cos \alpha + \cos \theta \sin \alpha \\ u_2 &= \cos \theta \cos \alpha - \sin \theta \sin \phi \sin \alpha \\ u_3 &= \sin \theta \cos \phi \cos \alpha + \cos \theta \sin \alpha \\ u_4 &= \cos \theta \cos \alpha - \sin \theta \cos \phi \sin \alpha \end{aligned} \quad (27)$$

$$\text{Since } \sum_{i=1}^n P_i e^{jks_i u_n} = f(u_n) e^{j\sigma} \quad (\text{equation (18) written in a}$$

more general form), equation (26) may be rewritten as

$$\begin{aligned}\vec{E} = & (u_1, -\sin \theta \cos \phi \cos \alpha, -\sin \theta \cos \phi \sin \alpha) f(u_2) e^{j(ka \sin \theta \sin \phi + \sigma)} \\ & + (\sin \theta \sin \phi \cos \alpha, -u_3, \sin \theta \sin \phi \sin \alpha) f(u_4) e^{j(ka \sin \theta \cos \phi + \sigma)}\end{aligned}\quad (28)$$

The  $E_\phi$  radiation pattern shall now be considered. The  $E_\phi$  field can readily be obtained from equation (28) since  $\vec{E} \cdot \vec{i}_\phi = E_\phi$ . Performing this operation one obtains

$$E_\phi = -u_5 f(u_2) e^{j(ka \sin \theta \sin \phi + \sigma)} - u_6 f(u_4) e^{j(ka \sin \theta \cos \phi + \sigma)} \quad (29)$$

where

$$\begin{aligned}u_5 &= \sin \theta \cos \alpha + \sin \phi \cos \theta \sin \alpha \\ u_6 &= \sin \theta \cos \alpha + \cos \phi \cos \theta \sin \alpha\end{aligned}\quad (30)$$

and where  $f(u)$  is still defined by equation (19) but may be written in the more general form

$$f(u_n) = \frac{\cos(m \cos^{-1} u_n)}{\sqrt{1 - u_n^2}} \quad n = 1, 2, 3, \dots \quad (31)$$

Each of the two terms on the right-hand side of equation (29) represents the radiation pattern for an antenna where the two antennas are located  $90^\circ$  apart on the circumference of the cone. From this equation the far-field pattern for one-way and two-way patterns can now be obtained.

For the one-way pattern, where the antennas are just transmitting (or receiving), the far-field pattern can be computed by taking the absolute value of  $E_\phi$  in equation (29).

$$\begin{aligned}|E_\phi| = & \left\{ \left[ u_5 f(u_2) \right]^2 + \left[ u_6 f(u_4) \right]^2 \right. \\ & \left. + 2u_5 f(u_2) u_6 f(u_4) \cos \left[ ka \sin \theta (\sin \phi - \cos \phi) \right] \right\}^{1/2}\end{aligned}\quad (32)$$



Where one antenna is receiving and the other is transmitting, the far-field pattern is obtained by multiplying the pattern of the transmitting antenna by the pattern of the receiving antenna. This two-way pattern can be computed from

$$|E_{\phi}| = u_5 f(u_2) u_6 f(u_4) \quad (33)$$

Similarly, the other two-way pattern, where each antenna acts as a transmitting-receiving antenna, can be computed by squaring equation (32).

$$|E_{\phi}| = [u_5 f(u_2)]^2 + [u_6 f(u_4)]^2 + 2u_5 f(u_2) u_6 f(u_4) \cos[ka \sin \theta (\sin \phi - \cos \phi)] \quad (34)$$

In equations (32), (33), and (34), account has to be taken of the change in elevation angle  $\theta$  of the major lobe when the antenna array is placed on a cone. As it stands,  $\theta$  is defined as the elevation angle with respect to the antenna array axis. As might be expected, when the array is placed on a cone, the elevation angle  $\theta'$  of the major lobe with respect to the cone axis takes on a different value. This angle value, a function of the half-cone angle  $\alpha$ , may be found from\*

$$\theta' = \cos^{-1} \left[ \frac{2 \cos \alpha \cos \theta + \sin \alpha \sqrt{1 + \cos^2 \alpha - 2 \cos^2 \theta}}{1 + \cos^2 \alpha} \right] \quad (35)$$

Therefore, to obtain the azimuthal patterns for arrays on a cone from equations (32) through (34), all  $\theta$ 's appearing in these equations must be replaced by  $\theta'$ .

## 6. RESULTS

Theoretical knowledge of the azimuthal coverage for one-way and two-way patterns for four slotted array antennas equally spaced around the circumference of a cone can now be obtained by computing the azimuthal

\*See appendix for derivation.

patterns as given in equations (32 through 34). To illustrate, a relative two-way azimuthal pattern is computed from equation (33) which uses a  $2 \times 2$  system. (A  $2 \times 2$  system is usually defined as a system where two transmitting antennas and two receiving antennas are alternated around the circumference of the cone or cylinder.) For this calculation, the antennas are assumed to be front fed\*\* with  $80^\circ$  as the elevation angle  $\theta$  of the main lobe. The half-cone angles  $\alpha$  considered are  $0^\circ$ ,  $5^\circ$ ,  $10^\circ$ ,  $15^\circ$ ; the corresponding elevation angles  $\theta'$  are  $80.0^\circ$ ,  $76.4^\circ$ ,  $72.8^\circ$ ,  $69.1^\circ$ .

The following cases were computed:

- a) Side-lobe level 50 db down ( $z_0 = 1.02483$ ), 30 slots ( $m = 29$ ),
- b) Side-lobe level 30 db down ( $z_0 = 1.01024$ ), 30 slots ( $m = 29$ ),
- c) Side-lobe level 30 db down ( $z_0 = 1.01379$ ), 26 slots ( $m = 25$ ).

As can be seen from figures 3 through 5, the relative azimuthal patterns, which are ideal, show that as the half-cone angle  $\alpha$  increases, the nulls become deeper and wider giving more and more the appearance of a clover leaf. That is, as the half-cone angle  $\alpha$  increases, the uniformity of the azimuthal coverage decreases.

In comparing the patterns for the above three cases, there appear no major differences in the patterns. The differences to be noted are the slight changes in the width and depth of the nulls and the appearance of some minor lobes.

Another two-way pattern, where each antenna is transmitting and receiving, is illustrated in figure 6. This two-way pattern, obtained from equation (34), is the square of the one-way pattern (equation 32). By plotting both these patterns in decibels, the two-way pattern will be two times that of the one-way pattern. If one were to draw the envelopes of these patterns, i. e., the curves touching just the maximum points, the resulting patterns would closely resemble the two-way patterns obtained from equation (33).

---

\*\* The values of  $\theta$  and  $\alpha$  that are actually used in the calculations are dependent on the definition of front feed (ref 2) and the geometry. Thus, the values of  $\theta$  and  $\alpha$  in the example become:  $\theta = -100^\circ$ ,  $\alpha = -180^\circ$ ,  $-175^\circ$ ,  $-170^\circ$ ,  $-165^\circ$ . There is no such difficulty with rear feed.

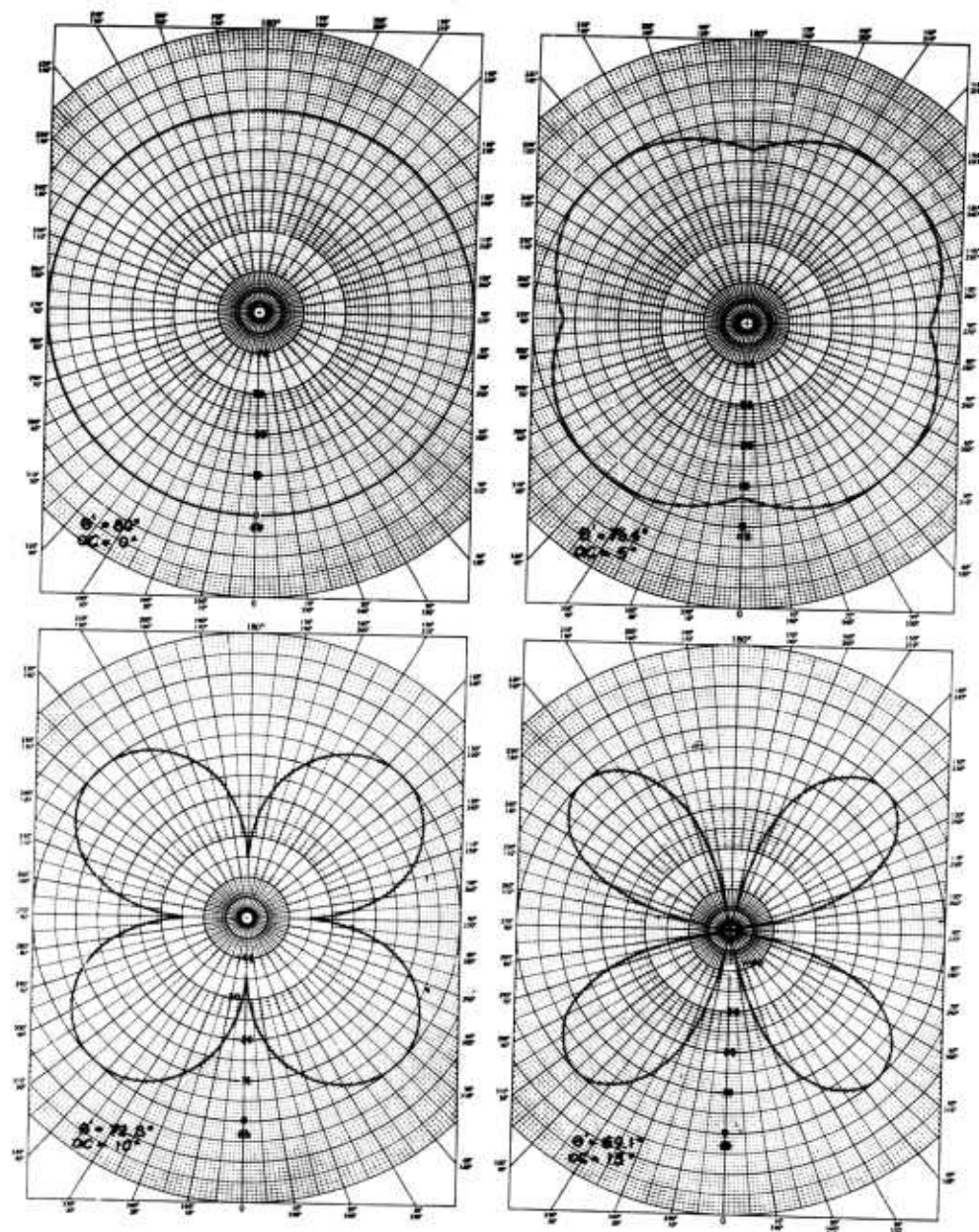


Figure 3. Two-way azimuthal patterns, example (a)

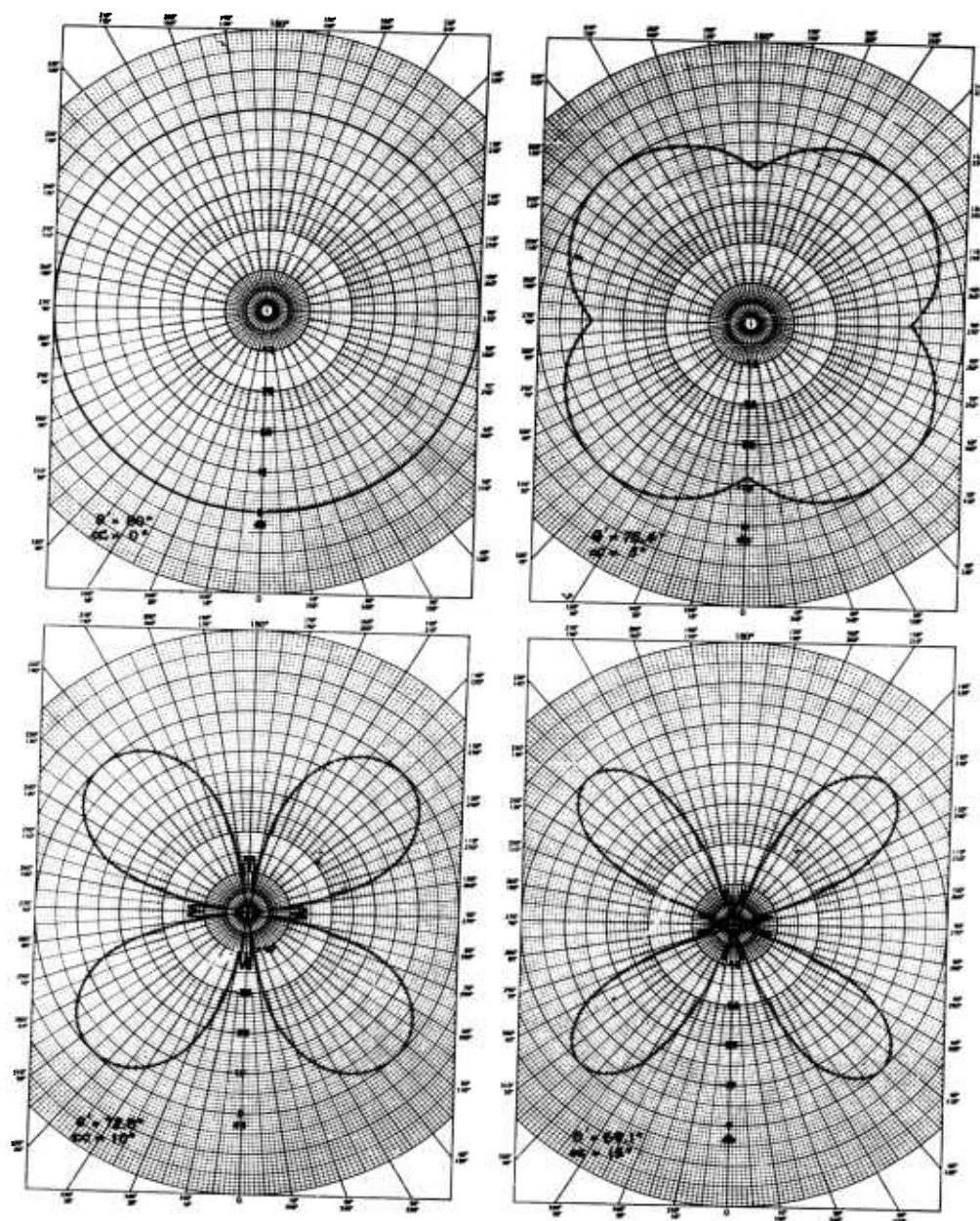


Figure 4. Two-way azimuthal patterns, example (b)

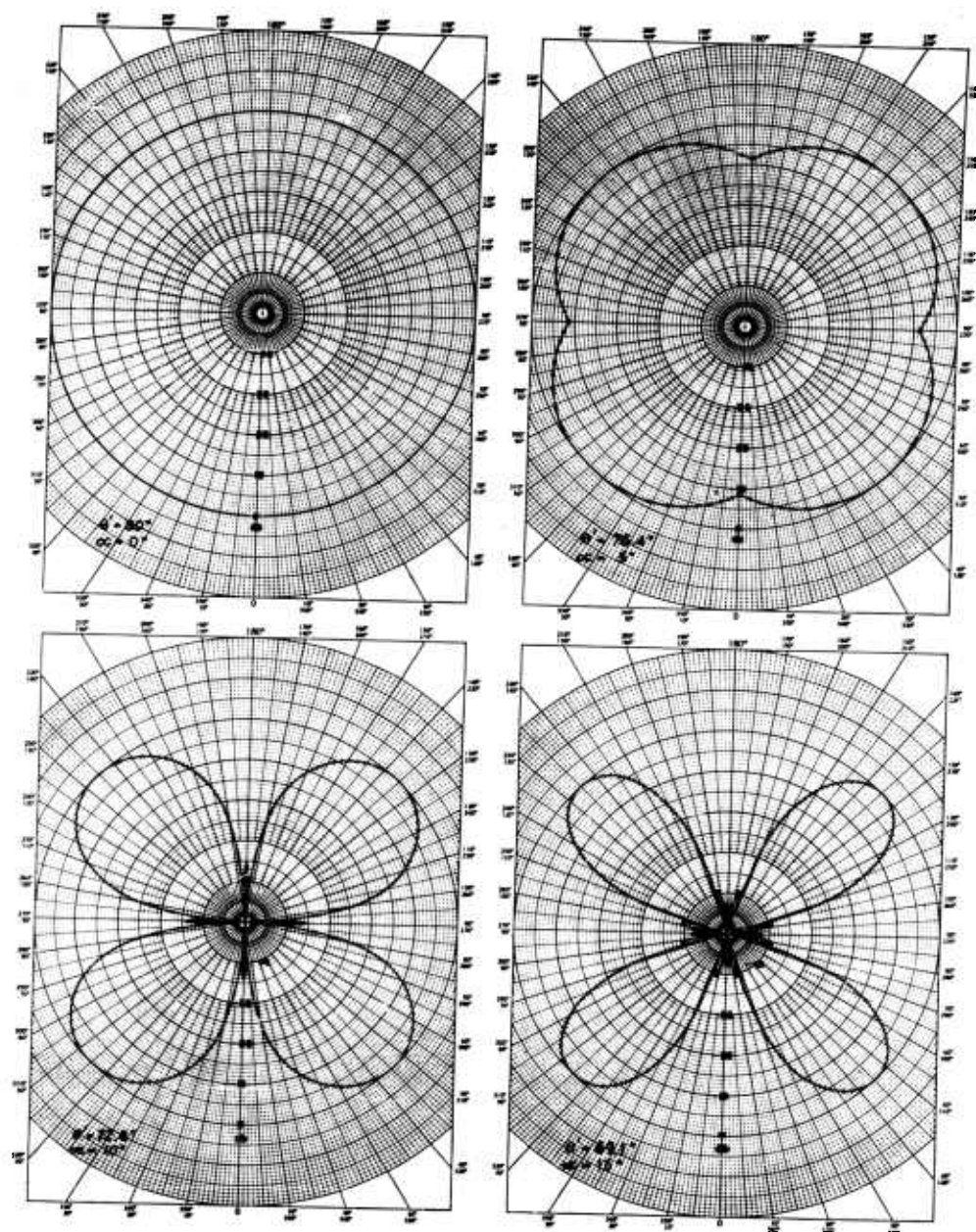


Figure 5. Two-way azimuthal patterns, example (c)



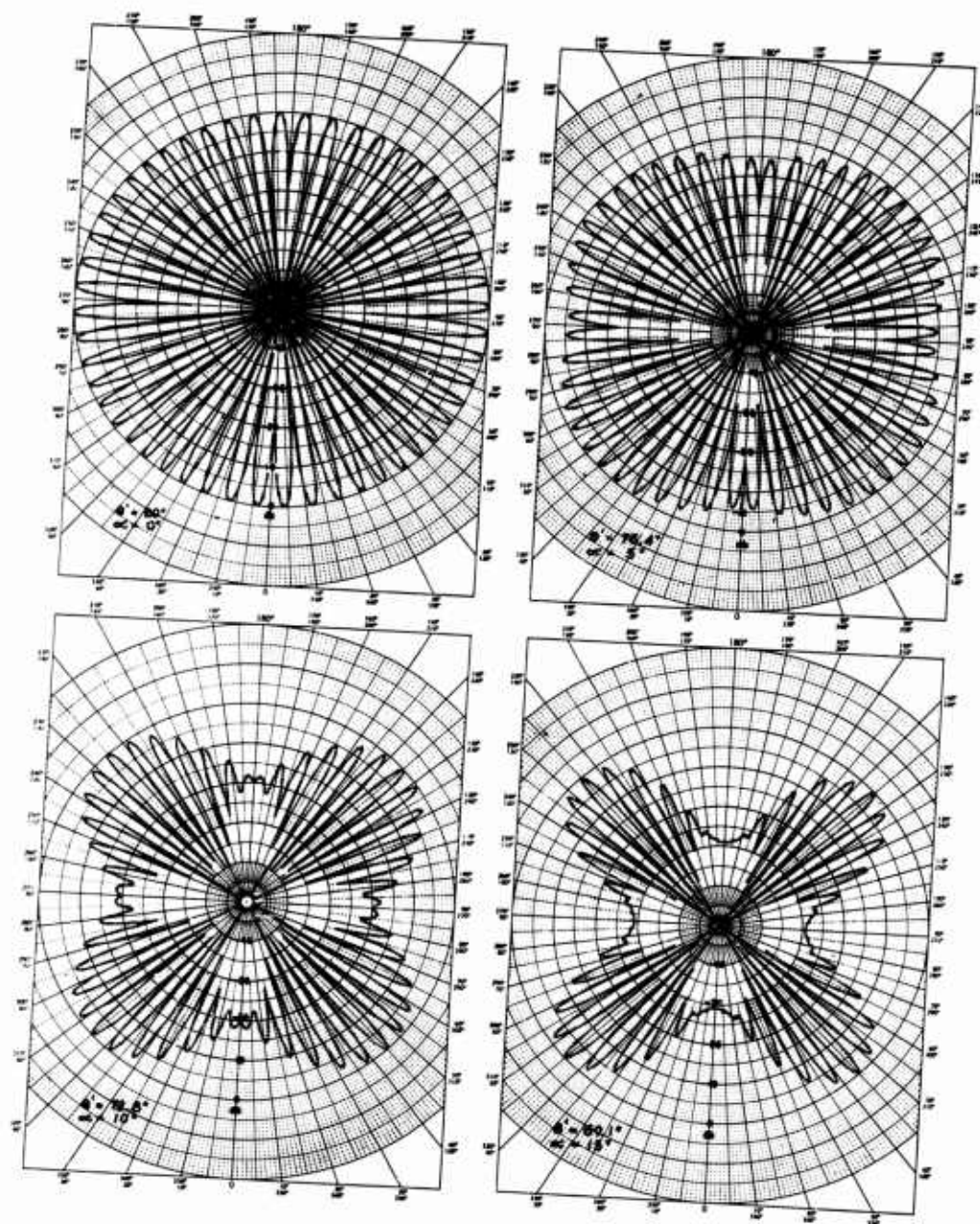


Figure 6. Two-way azimuthal patterns

Elevation patterns of the major lobes for  $2 \times 2$  systems, which were obtained experimentally, are shown in figures 7 through 11 with their respective azimuthal patterns presented in figures 12 through 16. As was pointed out in the previous section and shown in the elevation patterns, the value of the elevation angle  $\theta'$  of the major lobe is depended upon the half-cone angle  $\alpha$  (see also appendix). The azimuthal patterns show the same general shape of, and tendency toward, the cloverleaf appearance as the half-cone angle  $\alpha$  increases. Thus, the theoretical, relative azimuthal patterns confirm the azimuthal patterns that have been obtained experimentally.

## 7. CONCLUSION

The theoretical patterns obtained confirm the experimental patterns in that the nulls become deeper and wider as the cone half-angle increases; consequently, azimuthal coverage becomes less and less. If it is important to have azimuthal coverage as uniform as possible, then one must either try to keep the cone half-angle small, or increase the number of antennas on a cone (ref 4), or increase the beamwidth of the antennas.

By using a procedure similar to the one used in obtaining the far-zone field intensity for four antennas on a cone, one should be able to derive the azimuthal patterns for a lesser or a greater number of antennas.

## ACKNOWLEDGEMENT

The author wishes to thank Isadore Shapiro for obtaining the antenna patterns and Orval R. Cruzan and Whilden G. Heinard for their helpful suggestions and comments.

## 8. REFERENCES

1. Some Notes Concerning the Azimuthal Pattern of a Four-Element Transmitting Antenna Array for a Guided Missile Fuze, Franklin Fletcher, NBS Report 13.4-53R.
2. Designing an Optimum Linear Slotted Array Antenna, M. D. Prytulak, DOFL Report TR-550.
3. Instruction Manual for the 2-Way Antenna-Pattern Recorder, Henry C. Krason, DOFL Report TR-137.
4. Radiation Patterns as Related to Various Cone Shapes, Whilden G. Heinard, DOFL Report (in preparation).

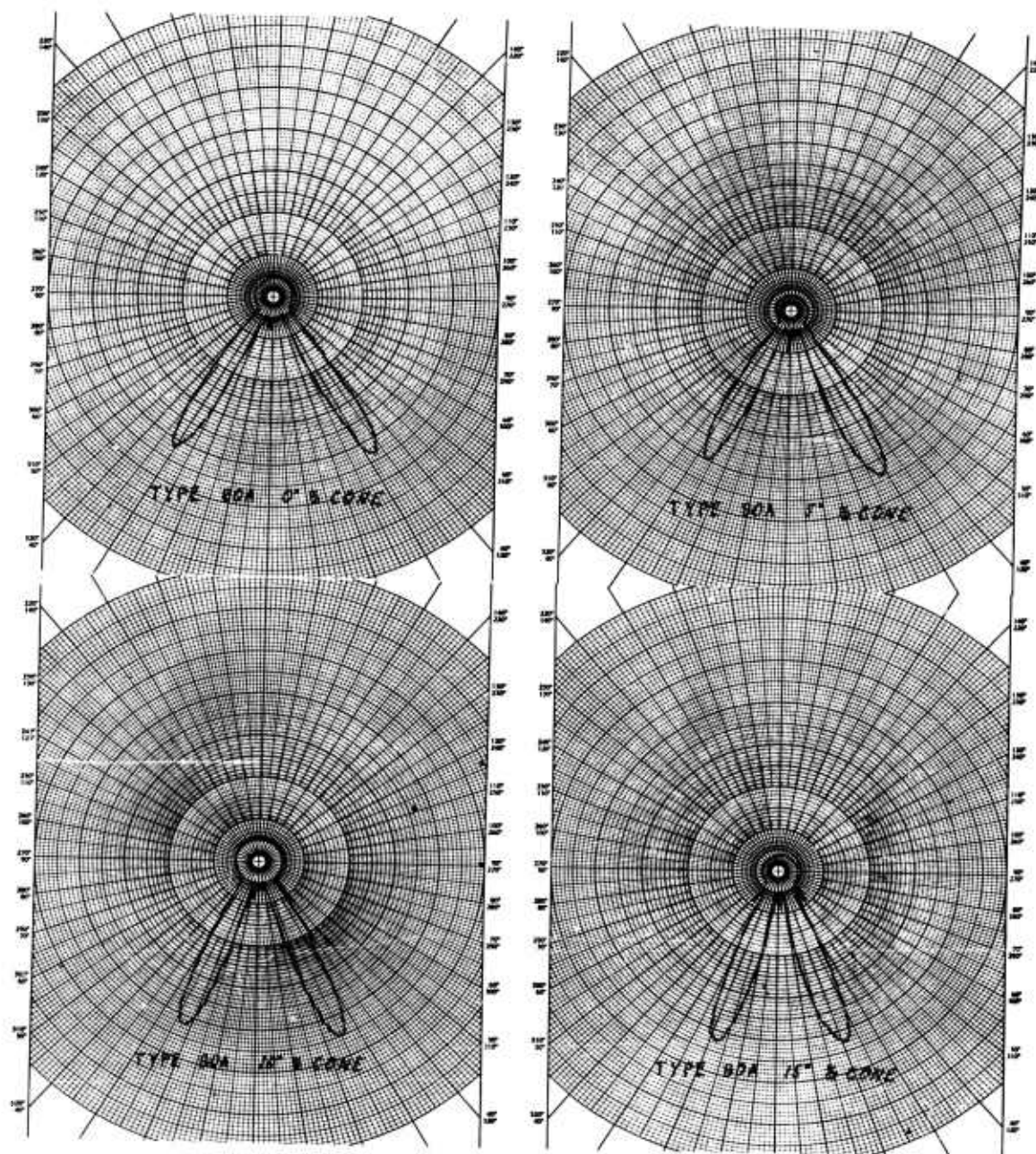


Figure 7. Elevation patterns, antenna type 80A



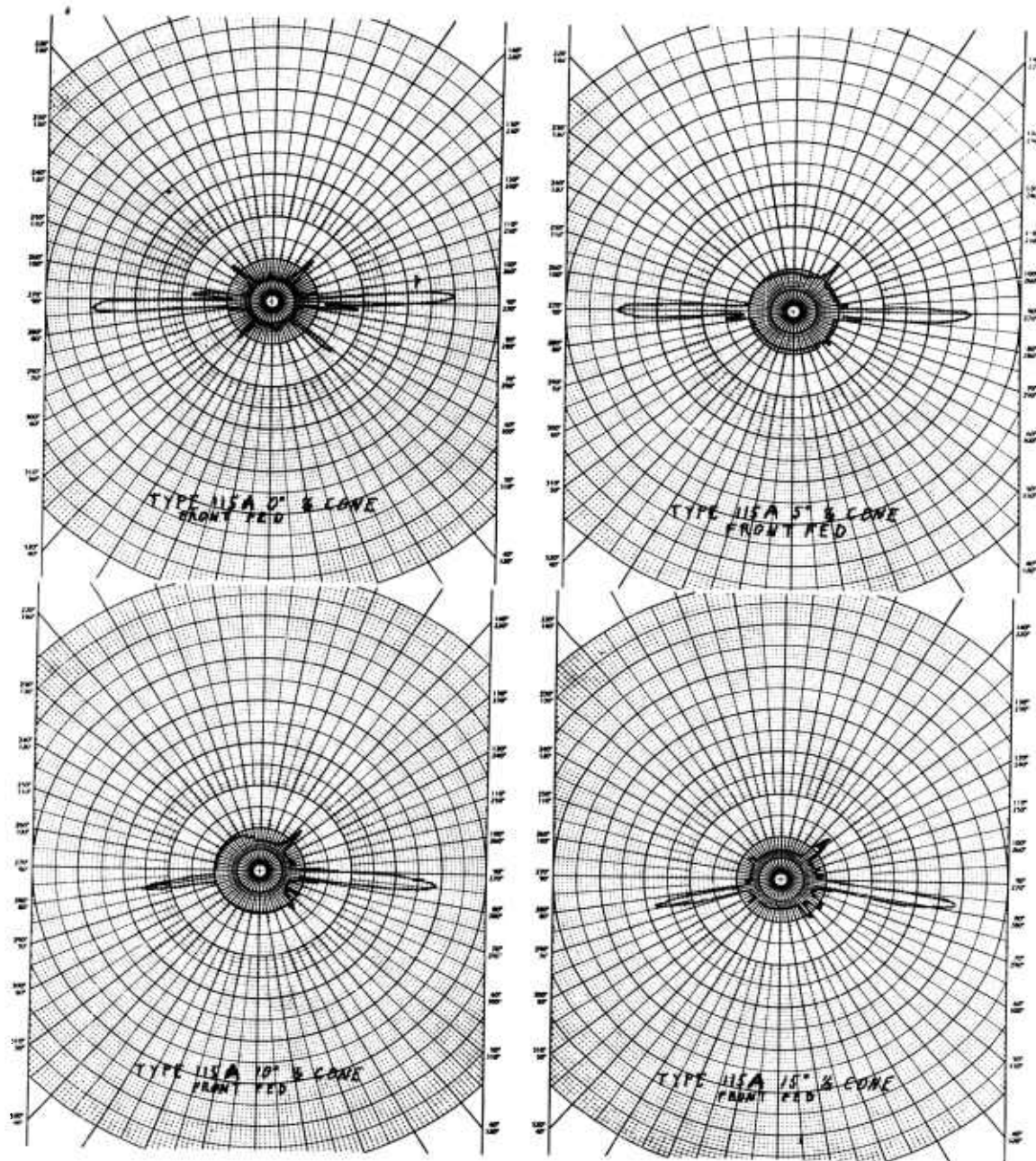


Figure 8. Elevation patterns, antenna type 115A, front fed

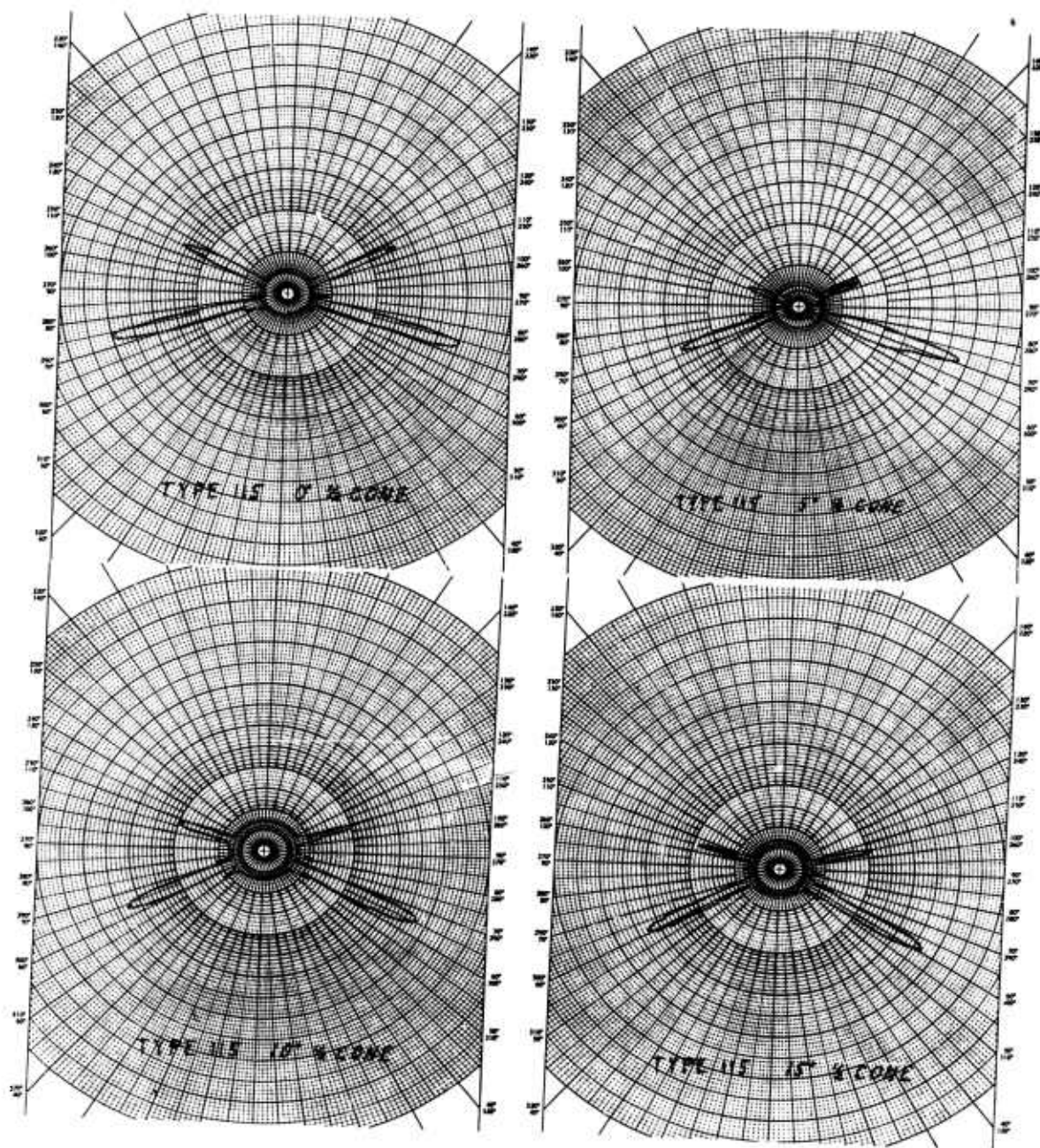


Figure 9. Elevation patterns, antenna type 115, rear fed

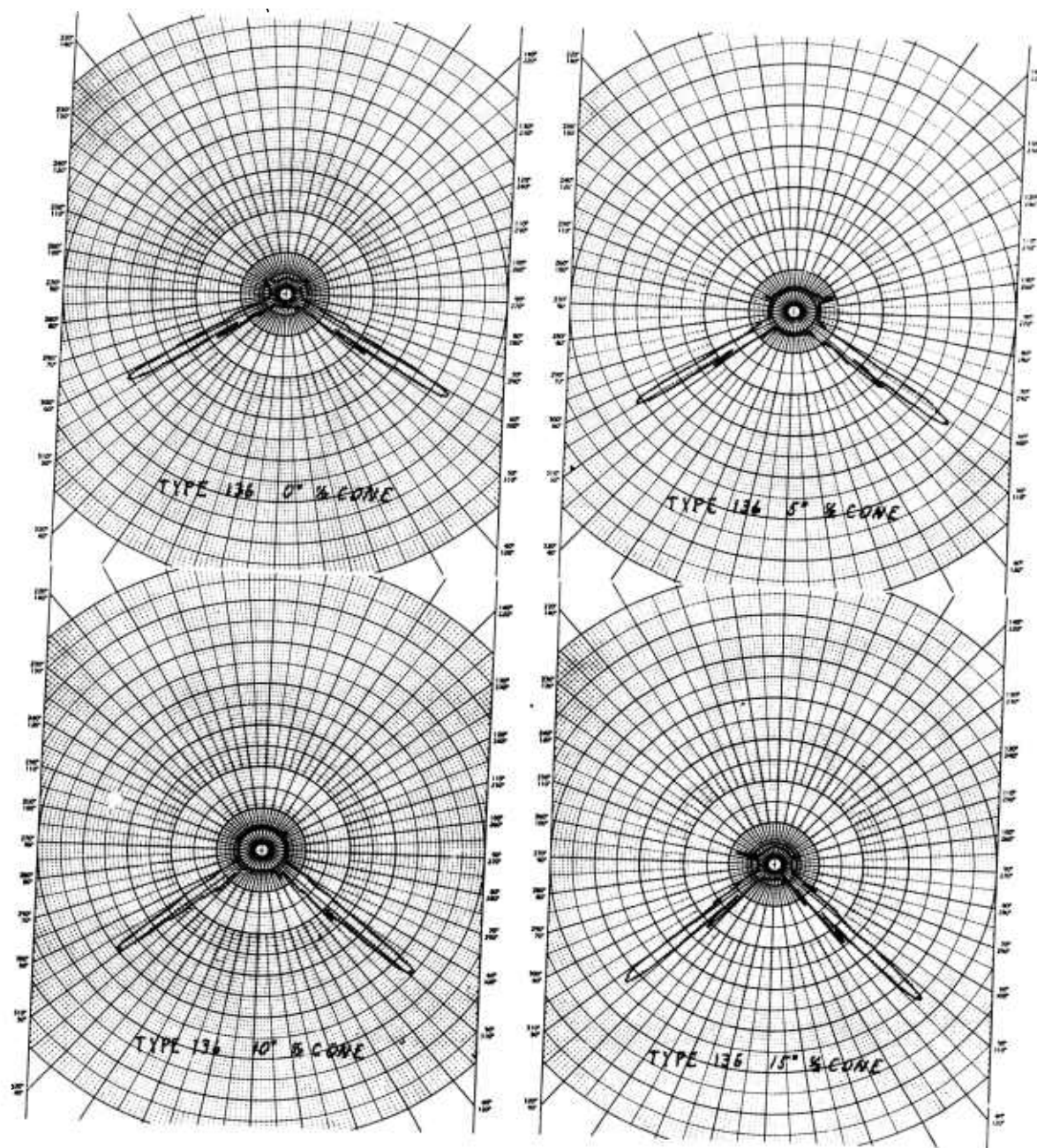


Figure 10. Elevation patterns, antenna type 136



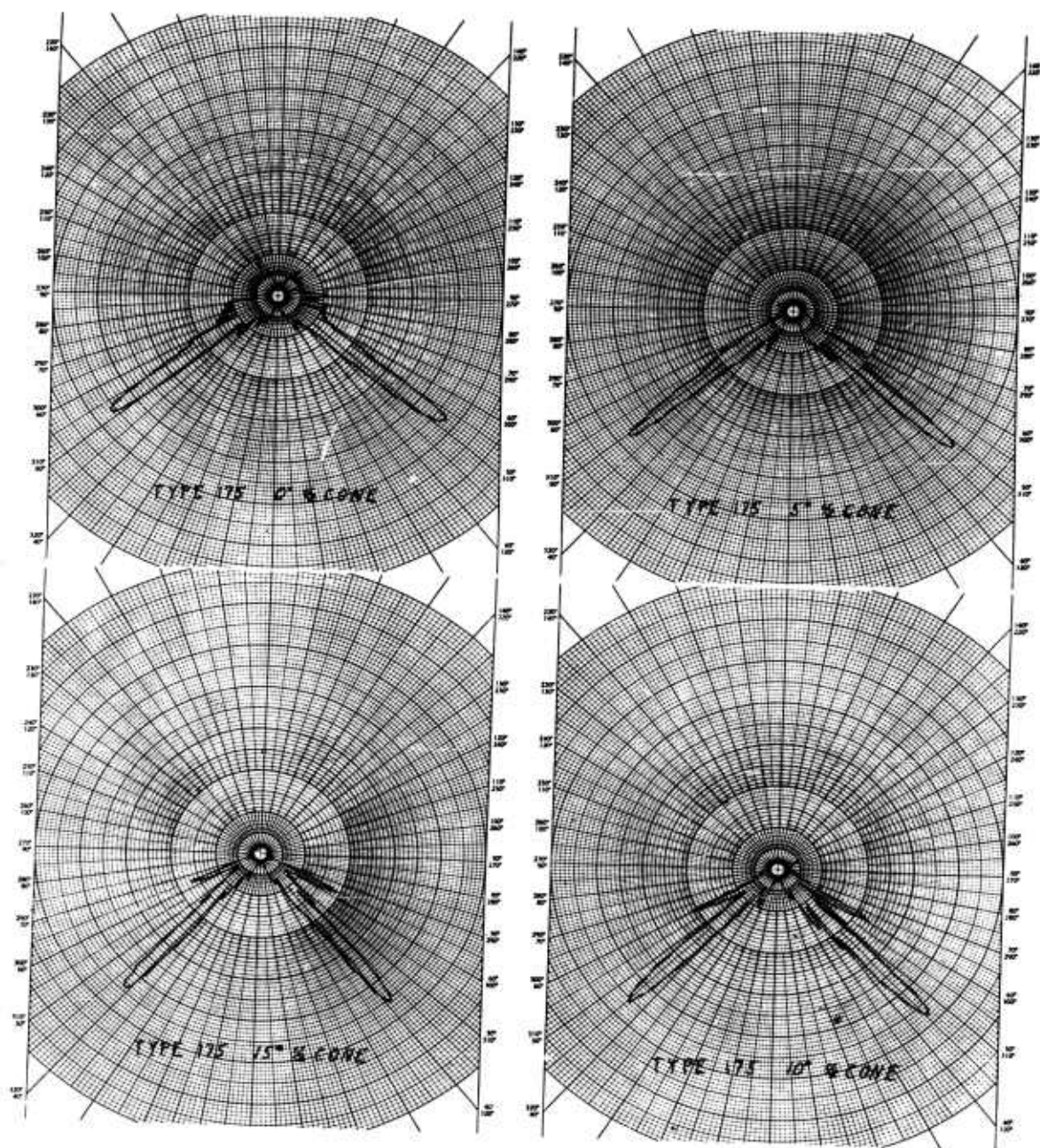


Figure 11. Elevation patterns, antenna type 175

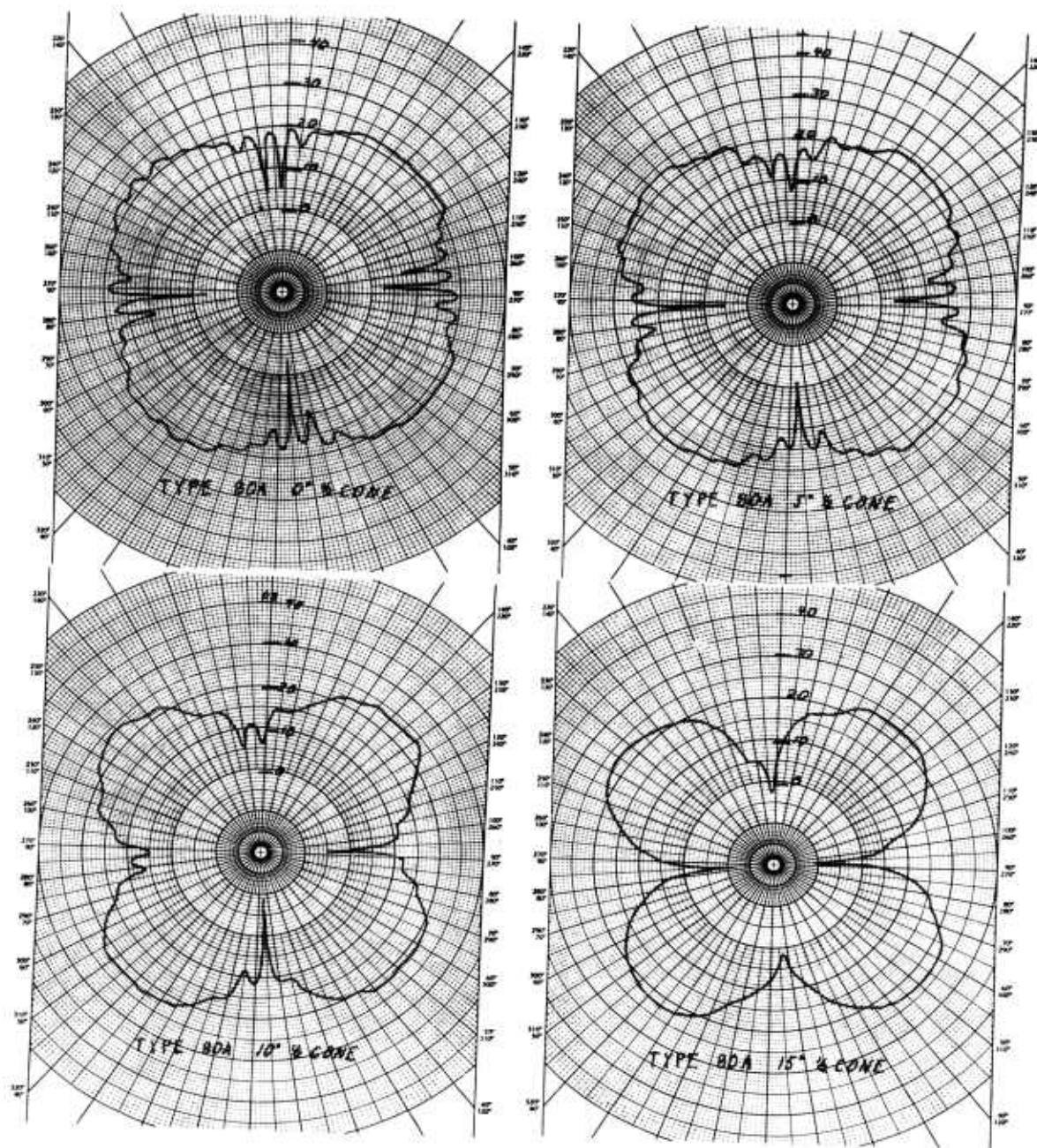


Figure 12. Two-way azimuthal patterns, antenna type 80A

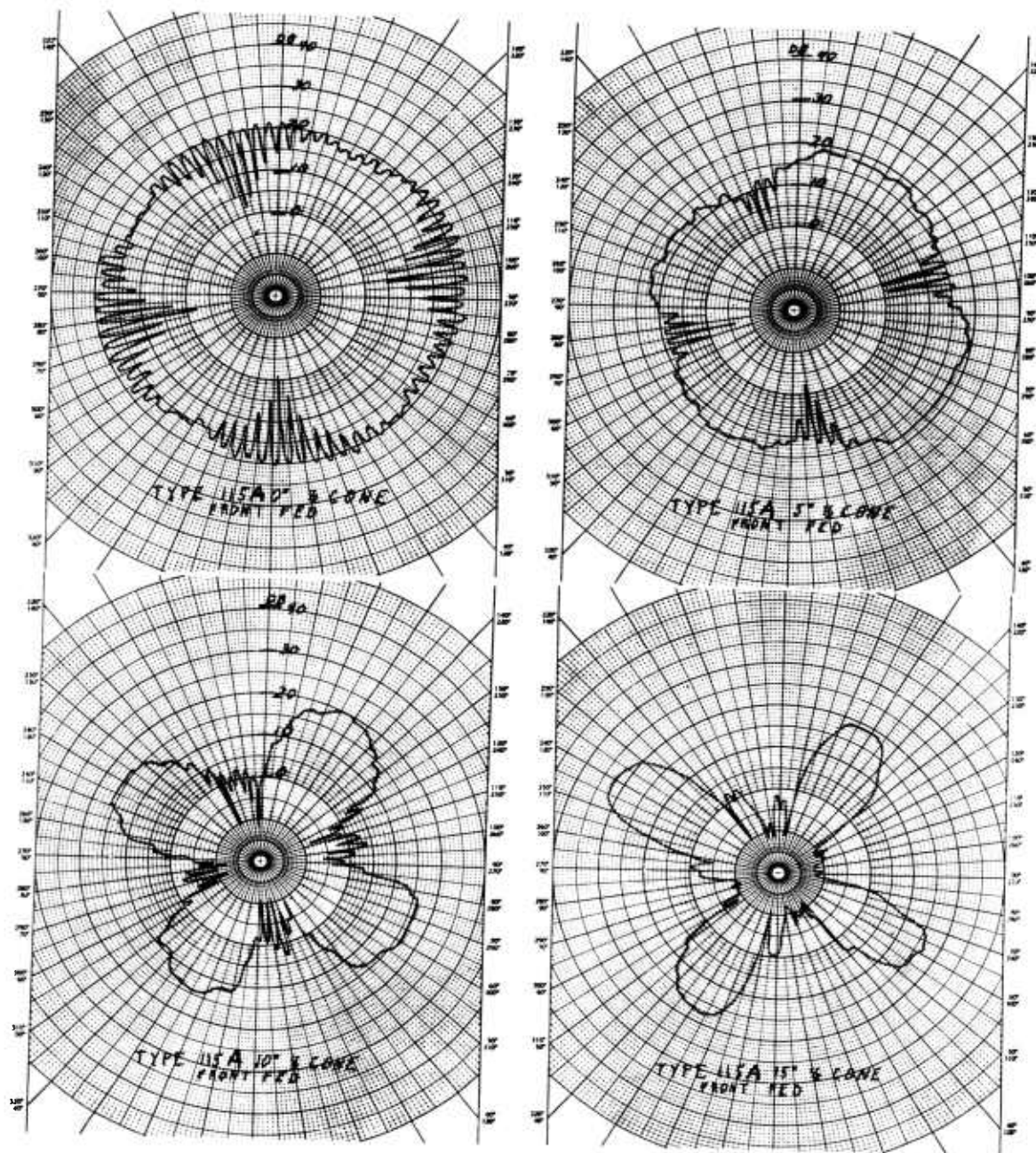


Figure 13. Two-way azimuthal patterns, antenna type 115A, front fed



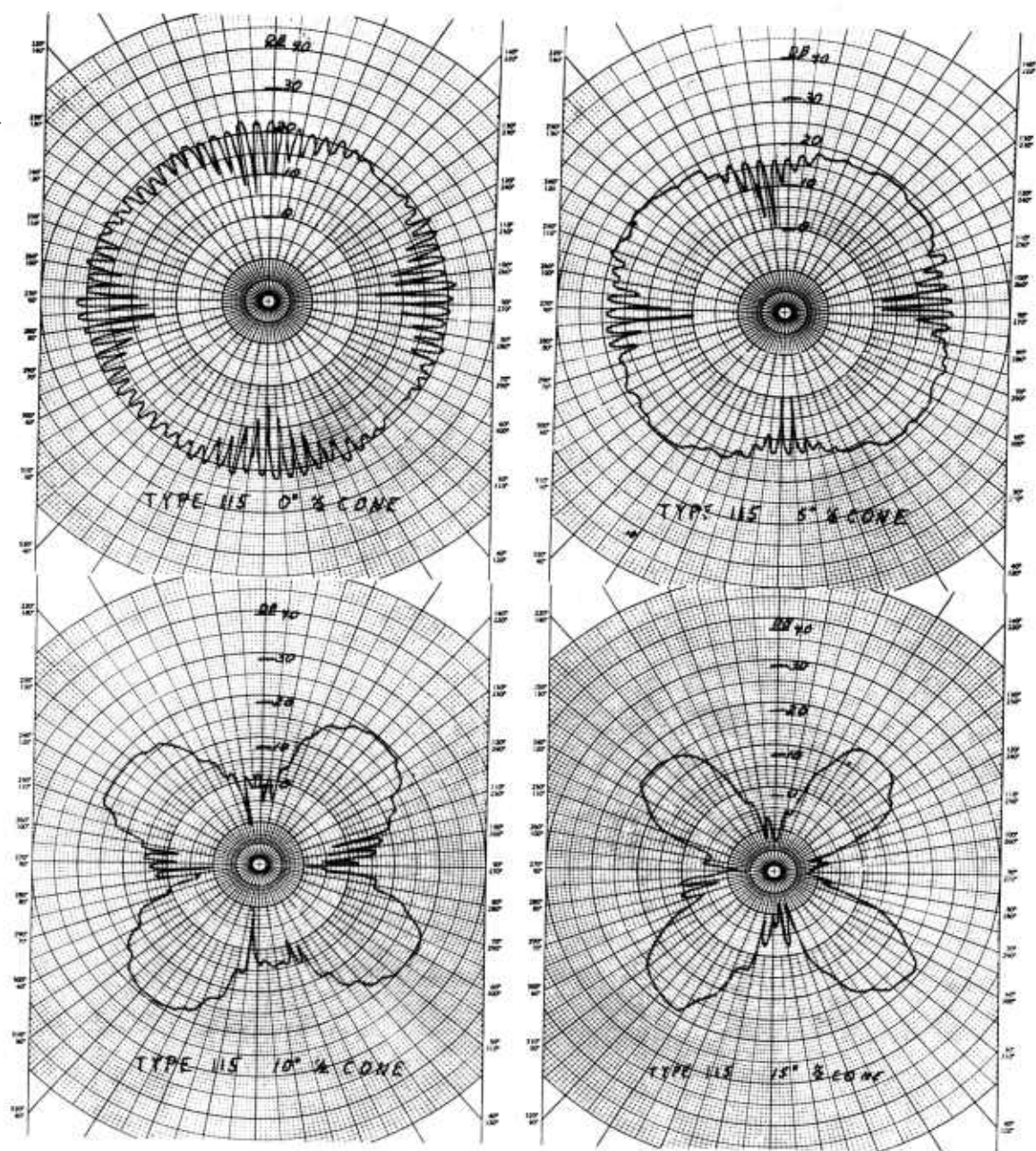


Figure 14. Two-way azimuthal patterns, antenna type 115, rear fed

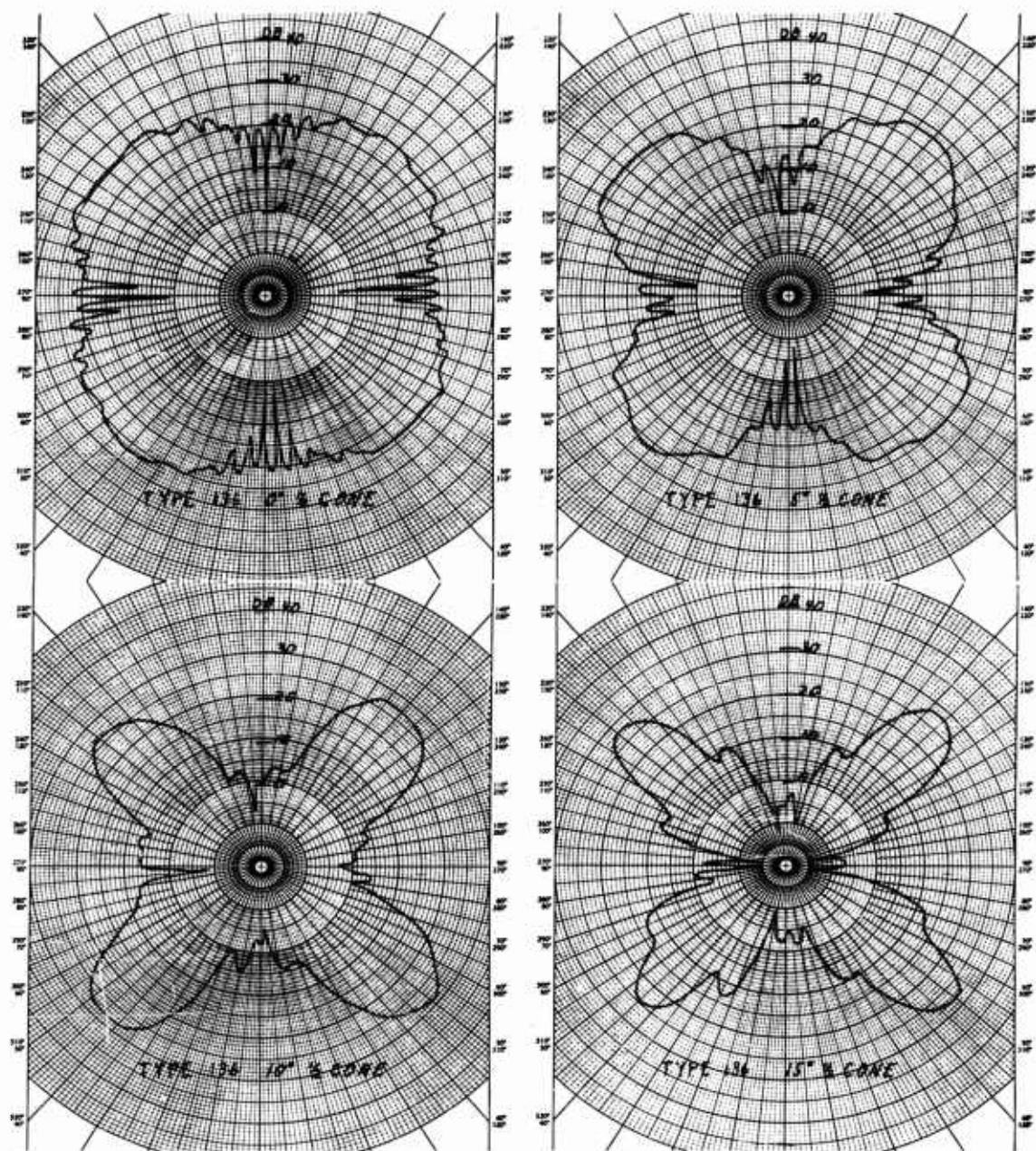


Figure 15. Two-way azimuthal patterns, antenna type 136



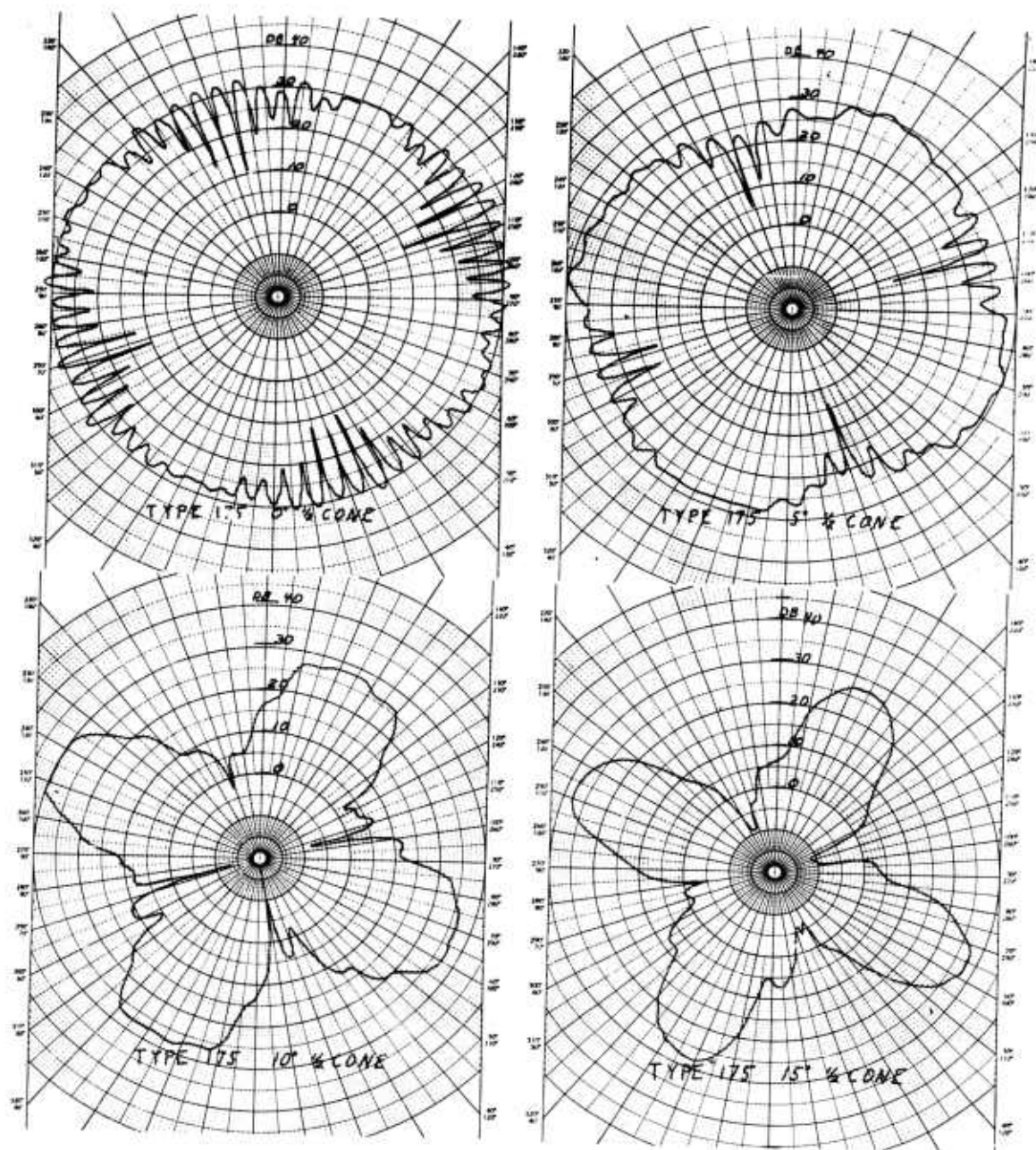


Figure 16. Two-way azimuthal patterns, antenna type 175

## APPENDIX

### ELEVATION ANGLE OF SLOTTED ARRAY ANTENNAS ON A CONE

The elevation angle of the major lobe of slotted array antennas is usually defined as the angle  $\theta$  formed by the center line of the major lobe with respect to the array axis. This definition, it would seem, complicates matters from a physical viewpoint when slotted array antennas are placed on a cone. A more appropriate definition perhaps would be: the elevation angle of the major lobe is the angle  $\theta'$  formed by the center line of the major lobe and the cone axis. Then the first definition becomes a special case, that of the degenerate case of a cylinder (cone half-angle  $\alpha = 0^\circ$ ). The elevation angles and the definitions become identical for this case since the cylinder axis and the array axis are either parallel or coincide.

In order to obtain the proper value of the elevation angle of the major lobe for the antennas on a cone as shown in figure 2, the effects of one antenna on the other and of the cone half-angle must be considered. Following is the derivation for this value.

In Figure A the unit radial vector  $\hat{i}_{r'}$  may be considered parallel to the axis of an antenna, while the unit vector  $\hat{i}_{r''}$ , which is in any plane containing both  $i_{r'}$  and  $i_{r''}$ , coincides with the direction of the axis of the major lobe. Expressed in terms of their Cartesian components, the radial vectors are

$$\hat{i}_{r'} = i_x \sin \alpha \cos \beta' + i_y \sin \alpha \sin \beta' + i_z \cos \alpha \quad (1)$$

$$\hat{i}_{r''} = i_x \sin \theta' \cos \phi + i_y \sin \theta' \sin \phi + i_z \cos \theta' \quad (2)$$

where

$\theta'$  = elevation angle of the major lobe with respect to the cone axis

$\alpha$  = cone half-angle

$\phi$  = azimuthal angles of the plane containing both  $i_{r''}$  and  $i_z$

$\beta'$  = azimuthal angles of the plane containing both  $i_{r'}$  and  $i_z$ ,

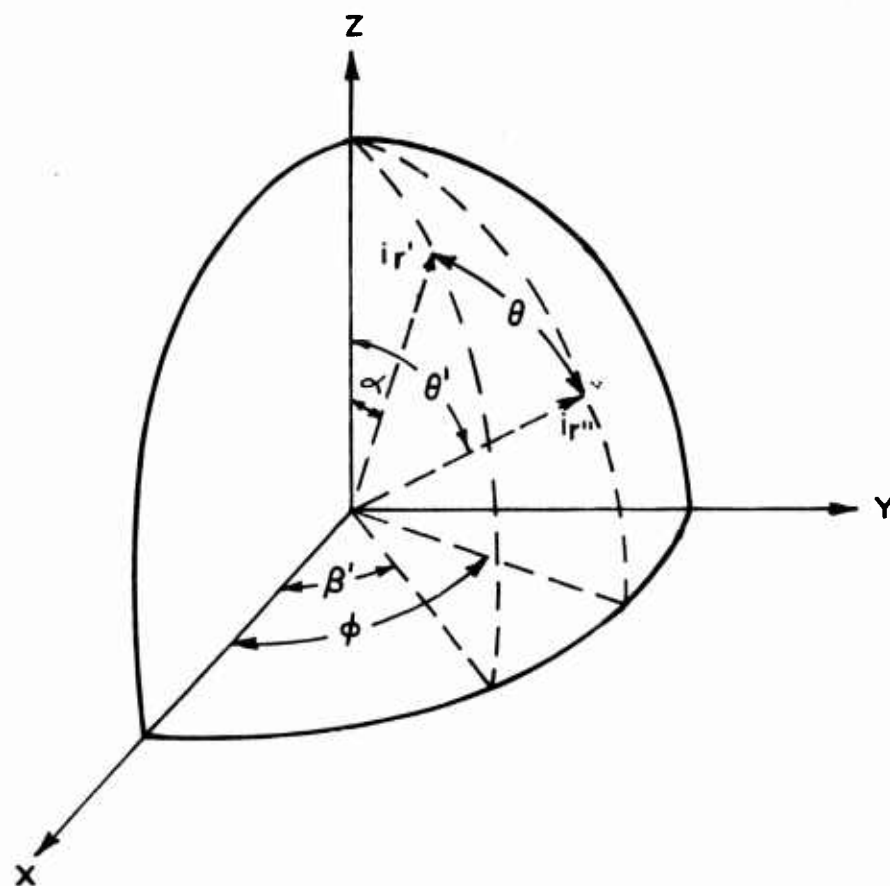


Figure A. Construction for finding the elevation angle of a slotted antenna on a cone

From figure A it is seen that

$$\cos \theta = \hat{i}_{r'} \cdot \hat{i}_{r''} \quad (3)$$

where  $\theta$  is the elevation angle of the major lobe with respect to the array axis. Performing this operation and using the expressions given by equations (1) and (2), one gets

$$\cos \theta = \sin \alpha \sin \theta' \cos (\beta' - \phi) + \cos \alpha \cos \theta' \quad (4)$$

Similarly, for another set of radial vectors,  $i_{r''}$  and  $i_{r'''} , one would obtain$

$$\cos \theta''' = \sin \alpha \sin \theta'' \cos (\beta'' - \phi) + \cos \alpha \cos \theta''. \quad (5)$$

Now let

$$\beta' = (3/2) \pi$$

$$\beta'' = \pi \quad (6)$$

$$\theta''' = \theta$$

which corresponds to having array one (1) in the yz-plane and array two (2) in the xz-plane as shown in figure 2, where both arrays lie on the surface of the same cone of half-angle  $\alpha$  and the elevation angles of the major lobes with respect to the antenna arrays are equal. Inserting the values of (6) into equations (4) and (5), one obtains

$$\cos \theta = -\sin \alpha \sin \theta' \sin \phi + \cos \alpha \cos \theta' \quad (7)$$

$$\cos \theta = -\sin \alpha \sin \theta'' \cos \phi' + \cos \alpha \cos \theta''. \quad (8)$$

Taking equation (7) and solving for  $\cos \theta'$ , one finds that

$$\cos \theta' = \frac{\cos \alpha \cos \theta \pm (2 \cos^2 \alpha \cos^2 \theta - \sin^2 \theta \sin^2 \alpha \sin^2 \phi)^{1/2}}{\cos^2 \alpha + \sin^2 \alpha \sin^2 \phi} \quad (9)$$

This equation gives for one slotted array antenna the value of the elevation angle  $\theta'$  of the major lobe with respect to the cone axis as a function of the azimuthal angle  $\phi$ . From equation (8) a similar solution is obtained for  $\cos \theta''$ .

The elevation angle  $\theta'$  for the antenna arrays, which is the result of the line of intersection of the loci of the major lobe axes, is obtained by noting that now

$$\theta'' = \theta' \quad \text{and} \quad \phi' = \phi. \quad (10)$$

Substituting these values into equation (8) and then taking the difference of equations (7) and (8), one obtains

$$0 = \sin \alpha \sin \theta' (\sin \phi - \cos \phi) \quad (11)$$

For Equation (11) to hold for all values of  $\alpha$  and  $\theta'$

$$\sin \phi = \cos \phi$$

$$\text{or} \quad \phi = (\pi/4) + n\pi. \quad (12)$$

Setting  $n = 0$  in expression (12), and substituting the value of

$\phi = \pi/4$  into equation (7), one obtains

$$\cos \theta = -(\sqrt{2}/2) \sin \alpha \sin \theta' + \cos \alpha \cos \theta' \quad (13)$$

Solve equation (13) for  $\cos \theta'$

$$\cos \theta' = \frac{2 \cos \alpha \cos \theta \pm \sin \alpha \sqrt{1 + \cos^2 \alpha - 2 \cos^2 \theta}}{1 + \cos^2 \alpha} \quad (14)$$

From the above equation the elevation angle  $\theta'$  as a function of the cone half-angle  $\alpha$  can be calculated.

For the purpose of examples the following table contains the experimental values  $\theta_E$  of the elevation patterns (figs 7 through 11) compared with the theoretical values of  $\theta'$  that were obtained from the above equation. (When the antenna array is on a cylinder,  $\alpha = 0^\circ$  and  $\theta' = \theta$ .)

TYPE \ $\alpha$	$0^\circ$	$5^\circ$	$10^\circ$	$15^\circ$
	$\theta_E, \theta'$	$\theta_E \quad \theta'$	$\theta_E \quad \theta'$	$\theta_E \quad \theta'$
80A	32.5 $^\circ$	28.5 $^\circ$ 28.8 $^\circ$	25 $^\circ$ 24.7 $^\circ$	21 $^\circ$ 20.2 $^\circ$
115A front fed	93 $^\circ$	89.5 $^\circ$ 89.5 $^\circ$	85.5 $^\circ$ 85.9 $^\circ$	82 $^\circ$ 82.3 $^\circ$
115 rear fed	74 $^\circ$	71 $^\circ$ 70.4 $^\circ$	66 $^\circ$ 66.8 $^\circ$	61 $^\circ$ 63.6 $^\circ$
136	58 $^\circ$	54 $^\circ$ 54.4 $^\circ$	51 $^\circ$ 50.6 $^\circ$	47 $^\circ$ 46.7 $^\circ$
175	52.5 $^\circ$	48.5 $^\circ$ 48.9 $^\circ$	46 $^\circ$ 45.1 $^\circ$	41 $^\circ$ 41.0 $^\circ$

# COMPLEMENTARY FILTERING

by

R. N. Johnson

G. R. Hickox

## ABSTRACT

A method has been developed for providing a low-distortion dc to 160-kc telemetry link. An FM/FM subcarrier is used for the d-c and low-frequency portions and direct FM for the high frequencies. Basically, a waveform of such frequency range is divided into two overlapping bands that are recombined with a minimum design error through use of complementary filtering and appropriate phase equalization.

Theoretical and mathematical investigations indicate that spectrum splitting and recombination without waveform distortion may be effected with a low-pass Butterworth filter and its high-pass counterpart provided (1) the filters are of odd order, and (2) phase equalization is correctly accomplished.

## 1. INTRODUCTION

Telemetering a continuous signal with a spectrum extending from dc to 160 kc can be performed by using an FM/FM subcarrier for the d-c and low-frequency portions and direct FM for the high frequencies. A scheme of this type is necessary since FM transmitters do not normally accommodate d-c information transmission except by using SCO's (sub-carrier oscillators); in addition, tape recorders normally require SCO's to record or play back d-c information.

Most important in the design of such a system is the manner in which the signal spectrum is split into low- and high-frequency portions. If complementary low-pass and high-pass filter functions can be found that are realizable, the two portions can be recombined into the data-reduction process (tape playback and waveform display). Thus, the waveform displayed is identical with the original waveform, whose spectrum is split to accomplish the transmission and recording.

## 2. COMPLEMENTARY FILTERING

### 2.1 System Techniques & Accuracy Requirements

Appendix A gives a detailed analysis of spectrum splitting and recombination without waveform distortion by using a low-pass Butterworth filter and its high-pass counterpart. This is effected, however, only if (1) the filters are of odd order, and (2) phase equalization is correctly accomplished.

The overall transfer function is an all-pass function of constant amplitude with the phase being a sum of inverse tangent functions. The resulting waveform distorting phase may be equalized<sup>1</sup> by appending all pass networks, which provide additional poles and zeroes as indicated in figure A-III. The positioning (and spacing) of the pole-zero array depends on the maximum design phase error together with the location of the poles and zeroes to be equalized.

Since the minimum frequency of the tape recorder is 250 cps and the maximum frequency of the discriminator is 10,500 cps, five octaves of overlap are available. Accuracy considerations demand a 40-db SNR (signal-to-noise ratio), thus requiring at least a third-order filter (appendix A).

The results given in appendix A indicate that the third-order Butterworth filter, with  $T_H$  taken as negative, is the easiest to phase-equalize. This is true because the spacing of the equalizing poles and zeroes is not determined by the complementary filter aspects alone. Guillemin's phase slope ripple factor (eq A-22) and "end-zone" effect relationships<sup>2</sup> (eq A-23) are used in determining the spacing. Knowledge of the required bandwidth<sup>3</sup> coupled with the above design information resulted in selecting a 7-kc frequency spacing ( $\Delta f$ ) for the pole-zero array, arranged in parallel lines 5 kc away ( $\sigma$ ) from the  $j\omega$ -axis.

<sup>1</sup> Guillemin, Ernst A., "Synthesis of Passive Networks," (John Wiley & Sons, Inc., 1957) p. 639.

<sup>2</sup> Guillemin, op. cit., pp 640-642

<sup>3</sup> DOFL Report No. TR-871, "Determination of Information Bandwidth Requirement for a TM System," R. N. Johnson, et al, 25 Jan 1961.

The maximum value of  $\sigma$  was restricted by a SCO cutoff at 10,500 cps. The minimum value was limited to the practicability of realizing the filter sections, particularly in the high-frequency (160 kc) region. A value of 5 kc for  $\sigma$  effected a good compromise between these limits, resulting in a negative real part that gave practical element values.

With the choice of the third-order Butterworth complementary filter and using a subtraction process,  $\Delta\omega$  may be fixed by design (fig. A-II). It is shown in appendix B that a lattice section is the best manner to accomplish the design of the equalization networks. Guillemin<sup>4</sup> proves that the angle between the  $j$ -axis and any complex zero may not exceed 45 deg if the conversion from a lattice section to the equivalent unbalanced configuration is attempted without the use of mutual inductive coupling or its equivalent. Since it is desirable to eliminate the need of such coupling in any network design,  $\Delta f$  must be at least 5 kc when the section closest to the origin is considered. The resultant change in phase slope ripple factor and departure from linearity at the end of the pass band as  $\Delta f$  is increased are shown in equations A-22 and A-23, respectively. Obviously, an increase of  $\Delta f$  is beneficial in that fewer filter sections would be needed to equalize out to 160 kc. These limits constrain  $\Delta f$  and a value of 7 kc was selected.

The phase slope ripple factor and end-zone effects of the above selections for  $\sigma$  and  $\Delta f$  are compatible with accuracy requirements (appendix A).

## 2.2 Design Problem

Since it is necessary to cascade many all-pass filter sections for the phase equalization, proper impedance matching must be provided to assure the characteristics of each section. It has been established that a constant resistance lattice section exhibits the necessary character,<sup>5</sup> while Guillemin<sup>6</sup> outlines the necessary bridged-T transformation for typical unbalanced configurations (appendix B).

<sup>4</sup> Guillemin, op. cit., p 260

<sup>5</sup> Zobel, Otto J., "Distortion Correction in Electrical Circuits with Constant Resistance Recurrent Networks," (Bell System Technical Journal, vol 7, p. 438, Apr 1928).

<sup>6</sup> Guillemin, op. cit., p. 239



The selected spacing requires 23 sections for the phase equalization. The section closest to the origin must be built as a twin-T circuit<sup>7</sup> (detailed in appendix B) in order that unobtainable negative parameters do not become necessary for the balanced-to-unbalanced configuration (eq B-5).

### 3. GENERAL APPLICABILITY

#### 3.1 Proper Order Selection (Butterworth Filter)

As stated in section 2, the two channels must have a region of frequency overlap. Knowing the design accuracy (expressible as SNR in terms of decibels) and frequency overlap, the order of filter may be calculated by the relationship

$$n = \frac{\text{SNR (in db)}}{3\Delta f \text{ (octaves overlap)}}$$

This results in the lowest order filter permissible; the other design criteria, however, may require the use of a higher-order filter. The higher order would allow a shift of the required overlap toward the higher frequencies of the available overlap area, often resulting in an easier overall solution of the phase equalization problem.

#### 3.2 Phase Equalization

Once the order of the complementary filter has been selected, the necessary phase equalization must be provided except in the trivial first-order case. Examination of the pole-zero pattern of the filter resultant indicates whether  $T_H$  should be taken as positive or negative to reduce the complexity of the phase equalization problem.

Frequency spacing may or may not be set by the complementary filter overall transfer function, depending on the order of filter. Distance from the  $j\omega$ -axis may then be chosen accordingly, remembering that this value should not exceed the frequency spacing. Specific values of these parameters are dictated by design phase slope ripple and end-zone effect requirements.

### 4. SUMMARY

The method described herein provides a low-distortion dc to 160-kc telemetry link. Waveforms of such wide frequency range may be divided

---

<sup>7</sup> Ibid

into two overlapping bands and recombined with a minimum of design error by utilizing complementary filtering and appropriate phase equalization.

In general, the development supplies design data for solving similar problems with varying parameters. The general applicability is detailed to aid in the practical solution of like problems.

## APPENDIX A

### MATHEMATICAL ANALYSIS OF BUTTERWORTH FILTER FUNCTIONS AND PHASE-EQUALIZATION FACTORS

#### 1. DERIVATION OF BUTTERWORTH FILTER FUNCTIONS

When a low-pass filter function is required, considerations of physical realizability<sup>8</sup> lead to an approximation of the form

$$|T_L|^2 = 1 / [1 + F^2(\omega)] \quad (A-1)$$

where  $|T_L|^2$  is the squared magnitude of the transmission through the filter and  $F(\omega)$  is some polynomial in  $\omega$  that approximates zero very closely for  $\omega < 1$  and grows large as rapidly as possible for  $\omega > 1$ . A simple change of variable

$$\omega = 1/\omega \quad (A-2)$$

converts eq (A-1) into a high-pass function.

$$|T_H|^2 = 1 / \left[ 1 + F^2\left(\frac{1}{\omega}\right) \right] \quad (A-3)$$

if eq (A-1) and (A-3) are complementary,

$$|T_L|^2 + |T_H|^2 = 1,$$

or

$$1 / [1 + F^2(\omega)] + 1 / \left[ 1 + F^2\left(\frac{1}{\omega}\right) \right] = 1 \quad (A-4)$$

$$1 + F^2(\omega) + 1 + F^2\left(\frac{1}{\omega}\right) = \left[ 1 + F^2(\omega) \right] \left[ 1 + F^2\left(\frac{1}{\omega}\right) \right] \quad (A-5)$$

$$2 + F^2(\omega) + F^2\left(\frac{1}{\omega}\right) = 1 + F^2(\omega) + F^2\left(\frac{1}{\omega}\right) + F^2(\omega) F^2\left(\frac{1}{\omega}\right) \quad (A-6)$$

<sup>8</sup> Guillemin, op. cit., p. 587.

The condition,

$$|T_L|^2 + |T_H|^2 = 1/(1 + \omega^{2n}) + \omega^{2n}/(1 + \omega^{2n}) = 1, \quad (A-15)$$

does not guarantee that a signal transmitted through two such filters in parallel and recombined will remain undistorted, unless the signals from the two filters are orthogonal. The form of the function used to realize Butterworth low- and high-pass filters is<sup>9</sup>

$$T_L = 1/D \quad (A-16)$$

$$T_H = \omega^n/D \quad (A-17)$$

where D has only the left half-plane roots of  $\omega^{2n} = -1$ .

Since  $j\omega^n$  is orthogonal to +1 only for n odd, any odd order Butterworth filter may be used, and the amplitude of

$$T_L + T_H = S \quad (A-18)$$

will be independent of frequency.

For distortionless transmission, it is also necessary that the transmission delay of S be independent of frequency. Putting eq (A-16) and (A-17) in (A-18),

$$1/D + \omega^n/D = S = (1 + \omega^n)/D, \quad (A-19)$$

it is evident that the zeroes of S fall at the zeroes of  $\omega^n = -1$ , whereas the poles (zeroes of D) fall at the left half plane roots of  $\omega^{2n} = -1$ . Thus for an n odd, the zeroes of D are alternately cancelled and mirrored in the j-axis by the zeroes of  $\omega^n = -1$ , starting with the zero at -1, with a resultant all-pass pattern for S. Figure A-1 represents this graphically for a fifth-order Butterworth function. (Proceeding as above, a third-order filter resultant would be as depicted in figure A-II.)

---

<sup>9</sup> Ibid

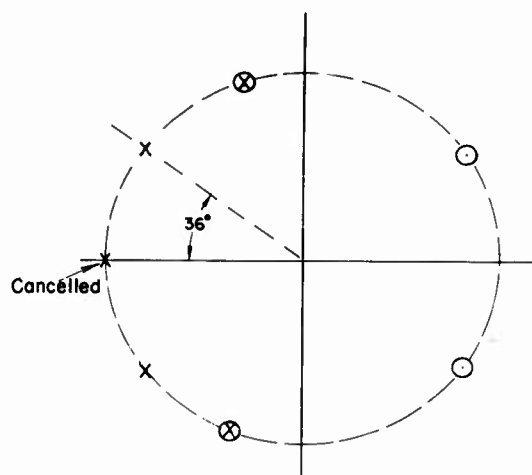


Figure A-I. Example of resultant fifth-order filter

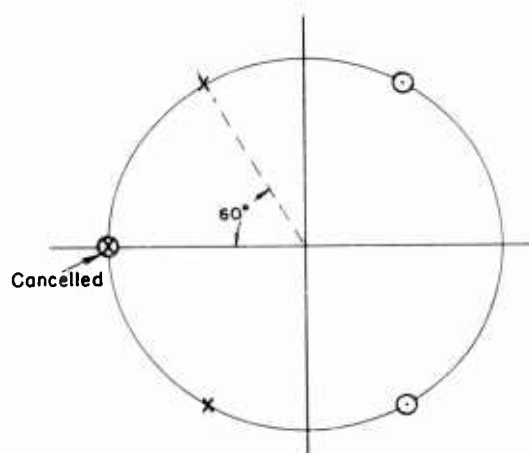


Figure A-II. Third-order Butterworth resultant

<sup>10</sup>Guillemin, op. cit., p. 659

These represent an all-pass transfer function of constant amplitude with the phase being a sum of inverse tangent functions. This phase, if left unattended, would distort the waveform being transmitted. As Guillemin shows,<sup>10</sup> the necessary linear phase equalization requires appending many all-pass sections to obtain equally spaced poles and zeroes in the overall transfer function (fig. A-III). These provide the additional phase that is sufficient to make the overall phase approximately linear, thereby making a constant time delay for all frequencies of interest.

Obviously, where the frequency spacing  $\Delta\omega$  (fig. A-III) is a small fraction of the overall bandwidth, many equalizing filter sections are required. It can be seen also that the singularities to be equalized should be located from the  $j$  axis as far as possible. Thus, the pole-zero patterns shown in figures A-I and A-II could present insurmountable equalization problems, because in each case  $\Delta\omega$  is fixed by the filter to be equalized, and the real part is less than the attainable maximum.

However, since  $T_H$  and  $T_L$  are orthogonal,  $T_H$  (or  $T_L$ ) may be taken as negative; thus,

$$|T_L|^2 - |T_H|^2 = 1 \quad (A-20)$$

For the case of  $T_H$  negative, the overall transfer function is described by

$$S = (1 - \omega^n)/D \quad (A-21)$$

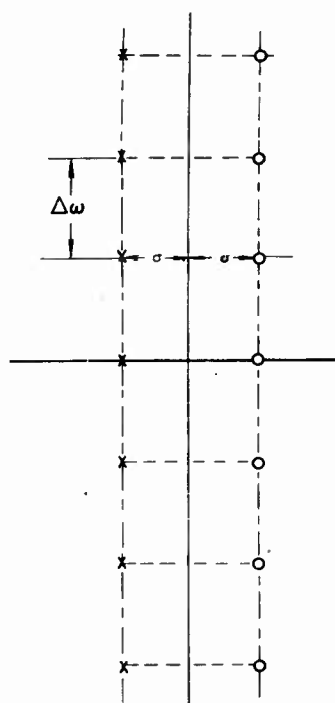


Figure A-III. Pole-zero array for linear phase approximant

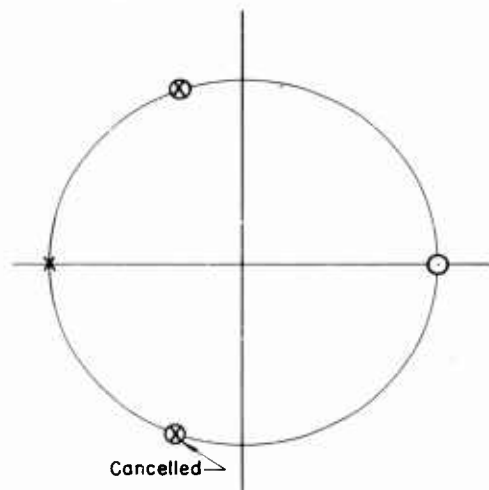


Figure A-IV. Example of third-order Butterworth resultant,  $T_H$  taken as negative

Now the numerator has zeroes at the  $n$ th roots of  $+1$  rather than  $-1$ , so that for a third-order function the resultant is as shown in figure A-IV. Thus, using the third-order Butterworth and considering  $T_H$  to be negative (subtracting in the recombination process) results in the simpler problem of phase equalizing a single pole and zero on the real axis. Since this does not affix a specific  $\Delta\omega$ , this value may be selected depending on design criteria. In addition, the value of  $\sigma$  is now at its maximum (normalized), which requires the minimum possible  $Q$  for each equalizing filter section. Considering the equalizing problem, it is easily seen that if a seventh-order filter were required, the recombination would be additive; subtractive for ninth order, etc. The higher order filters, however, would require two or more parallel arrays of both poles and zeroes for the phase equalization.

Selection of the proper order of complementary filter is contingent first on the amount of overlap available for the two channels to be recombined. Obviously, the only effects experienced by the signals must be those due to the complementary filters alone, with the practical relaxation that in the frequency range where a signal is contributing less than the ambient noise level, it may be ignored. This condition defines an overlap region where both channels are frequency independent, which may be approximately (within one octave) specified in terms of SNR (signal to noise ratio) in db and order  $n$  of filter as

$$\text{Octaves of overlap} = \text{SNR}/3n \quad (\text{A-22})$$

This overlap criterion sets the minimum allowable order of filter.

If the accuracy requirement and available overlap are such that a fifth or higher order filter is needed, the maximum frequency spacing ( $\Delta\omega$ ) and the real part value ( $\sigma$ ) are set by the filter characteristics. However, if a third-order filter is permitted,  $\Delta\omega$  is not set by the filter to be equalized, but by other design criteria. Building an infinite array of phase equalizing poles and zeroes is not considered practicable; analysis must be made of the effects of providing only a finite number of discretely placed singularities.

## 2. PHASE-EQUALIZATION FACTORS

Guillemin<sup>11</sup> shows that the phase slope ripple factor, when  $\sigma$  is small in comparison with the entire bandwidth, is approximately equal to

$$2e^{-2\pi\sigma/\Delta\omega} \quad (\text{A-23})$$

For example, substituting the values of 7 and 5 for  $\Delta\omega$  and  $\sigma$ , respectively, for possible third-order-filter design results in a ripple factor of about 2 percent.

The amount of the phase slope would drop below normal (due to the noninfinite array) is approximately equal to<sup>12</sup>

$$\frac{\sigma}{\Delta\omega} \ln(2n\Delta\omega/\sigma) \quad (\text{A-24})$$

The example of covering an information bandwidth of 160 kc with 7-kc frequency spacing would demand 23 sections for the above third-order filter equalization.

The results of eq (A-2) for the above parameters give a value of 2.94, which is the drop in linear phase slope at the band limit. This value is small compared with  $23\pi$  which results in a value of 72.3. This drop in magnitude (about 4 percent) may be lessened by extending the pole pattern, or by empirically inserting several extra sets of poles and zeroes near the high-frequency end. An extension of the pattern would demand some 35 filter sections (an increase of 12) to improve this figure to less than 3 percent.

In this case it would not only mean considerably more circuitry, but that the highest frequency pole would be at 225 kc, resulting in a design that would be hard to build. Therefore, the linear phase slope

<sup>11</sup> Guillemin, op. cit., p. 640

<sup>12</sup> Guillemin, op. cit., p. 642

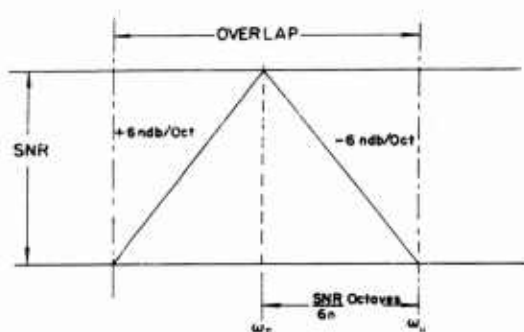


Figure A-V. Overlap region

is improved best at the high-frequency end by crowding in whatever additional singularities that are found necessary.

For a fifth-order filter, the maximum phase slope ripple factor would be 0.87 percent (eq A-23), since the maximum  $\Delta\omega$  and the value of  $\sigma$  are set by the filter characteristics. A need for greater phase slope ripple accuracy would require closer frequency spacing; hence, many more all-pass sections for a given bandwidth. The disadvantages of the

fifth-order filter are (1) the frequency spacing is set by the filter to be equalized (not necessarily the maximum design error), and (2)  $\sigma$  is smaller than the maximum possible real part value (i.e., when the singularities to be equalized lie on the real axis as in the third-order case).

Although the overlap criterion may permit a third-order filter, the choice of a fifth order might be better. The use of the higher order filter, when several extra octaves of overlap are available (as would be the case if the third-order filter were permissible), would allow the crossover frequency to lie higher in the overlap region. This might obviate the smaller real part difficulty. A direct analysis of crossover frequency ( $\omega_c$ ) vs filter order may be made as follows: (Figure A-V shows the general relationships needed.)

$$\omega_c = \frac{\omega_u}{2^{\text{SNR}/6n}} \quad (\text{A-25})$$

gives the crossover frequency in terms of the upper frequency limit ( $\omega_u$ ). For a higher crossover frequency as would be allowed by a higher order filter,

$$\omega'_c = \frac{\omega_u}{2^{\text{SNR}/6n'}} \quad (\text{A-26})$$

Therefore,

$$\omega'_c / \omega_c = \frac{\frac{\omega_u}{2^{\text{SNR}/6n'}}}{\frac{\omega_u}{2^{\text{SNR}/6n}}} \quad (\text{A-27})$$



which

$$= \frac{2^{\text{SNR}/6n}}{2^{\text{SNR}/6n'}} \quad (\text{A-28})$$

Finally,

$$\omega_c' / \omega_c = 2^{\text{SNR}(n' - n)/6nn'} \quad (\text{A-29})$$

A comparison of the third-and fifth-order filters shows that if the SNR is high enough, a fifth-order filter could be used that would still have a real part ( $\sigma$ ) equal to, or even greater than, the third-order filter. As stated, the fifth-order filter fixes  $\Delta\omega$  in addition to the relative value of  $\sigma$ . Thus, the phase slope ripple factor (eq A-23) for a fifth-order filter has a maximum value (0.67 percent) that, for many applications, may be less than the required design accuracy. Therefore, since more sections would have to be built for a desired bandwidth than in the third-order case where  $\Delta\omega$  may be made greater, it can be seen that the third-order filter should be used when a higher ripple factor is permissible and the overlap criterion is satisfied.

## APPENDIX B

### REALIZATION OF PHASE-EQUALIZATION NETWORKS

#### 1. CONSTANT RESISTANCE LATTICE

The constant resistance lattice shown in figure B-I provides proper impedance matching when many sections are cascaded.

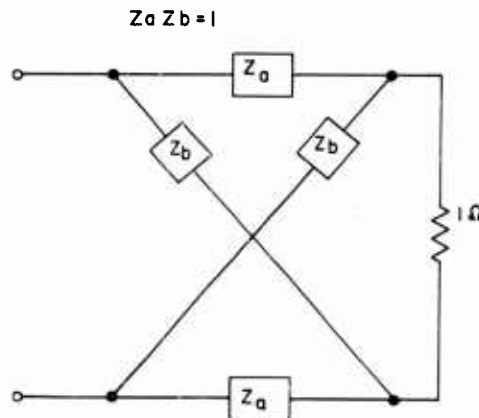


Figure B-I. Constant resistance lattice section

To obtain a conjugate set of both poles and zeroes necessary in each of the phase equalization networks, each lattice impedance,  $Z_a$  and  $Z_b$ , must contain an inductance and capacitance. The input impedance is a constant 1 ohm, since the section is terminated in 1 ohm. The impedances are constrained so that  $Z_a Z_b = 1$  (fig. B-II).

Observing the 1-ohm termination, the voltage-transfer function<sup>13</sup> is given by the following

$$Z_{12} = E_2/E_1 = E_2/I_1 = (1 - Z_a)/(1 + Z_a) \quad (B-1)$$

$Z_{12}$ , for a conjugate set of poles and zeroes as shown in figure B-III, is given by

$$\frac{s^2 - 2as + b^2}{s^2 + 2as + b^2} \quad (B-2)$$

Solving eq (B-1) for  $Z_a$ , substituting (B-2), and simplifying results in

$$Z_a = 2as/(s^2 + b^2) \quad (B-3)$$

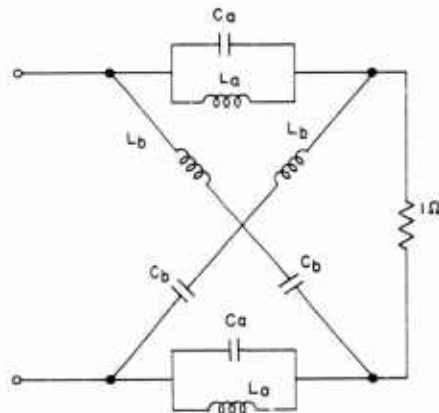


Figure B-II. Constant resistance lattice network

<sup>13</sup> Guillemin, op. cit., p. 478

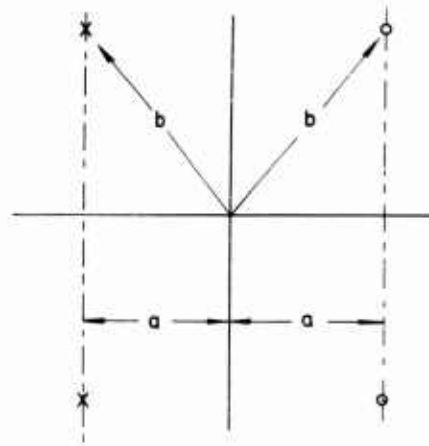


Figure B-III. Conjugate pole-zero pattern for one filter section

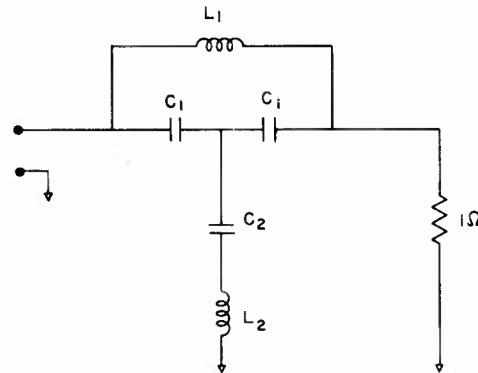


Figure B-IV. Bridged-T network

## 2. THE BALANCED-TO-UNBALANCED CONFIGURATION TRANSFORMATION

The equivalent unbalanced bridged-T network to which each designed lattice section must be converted is shown in figure B-IV. The following relationships govern the simple transformation<sup>14</sup>

$$L_1 = 2L_a \quad (\text{B-7})$$

$$C_1 = C_a \quad (\text{B-8})$$

<sup>14</sup> Guillemin, op. cit., p. 259

$Z_b$ , being the reciprocal of  $Z_a$ , is

$$Z_b = (s^2 + b^2)/2as \quad (\text{B-4})$$

$Z_a$  is recognized as a simple parallel LC circuit that has the form

$$Z = \frac{s/C}{s^2 + 1/LC} \quad (\text{B-5})$$

Comparably,  $Z_b$  is a series LC circuit with Z form of

$$Z = \frac{s^2 + 1/LC}{s/L} \quad (\text{B-6})$$

The values of  $C_a$  and  $L_a$  are easily calculated from the above for each lattice section if the placing of the singularities has been rigidly set at a specific  $\sigma$  from the  $j\omega$ -axis at a frequency spacing of  $\Delta\omega$ . Obviously,  $C_b$  and  $L_b$  are equal to  $L_a$  and  $C_a$ , respectively. At the time of unnormalizing, the impedance level is also suitably changed.

$$L_2 = L_b/2 \quad (B-9)$$

$$C_2 = 2C_a C_b / (C_b - C_a) \quad (B-10)$$

The configuration is realizable provided the inequality  $C_a/C_b \geq 1$  is satisfied. If, for instance, this inequality is not satisfied for the lowest frequency section, it must be realized by a lattice to twin-T transformation<sup>15</sup>. However, since it has been established that no complex zeroes of transmission are farther from the  $j$ -axis than 45 deg (appendix A), this new transformation is feasible and practical without mutual inductive coupling.

---

<sup>15</sup> Ibid

# A NEW ELECTROCHEMICAL SYSTEM FOR HIGH-VOLTAGE, LOW CURRENT DRAIN APPLICATIONS

by

William J. Pauli

## ABSTRACT

A new battery system has been designed for miniature high-voltage, low-current drain applications. The battery, a stack of cells that are 1/2 in. in diameter and 0.013 in. thick, provides 60 v/in. of length. The capacity is 5 coulombs and the drain rate 0.1 to 10  $\mu$ a. The unit operates over the temperature range -65°F to +165°F; several stored at +125°F for more than a month showed very slight loss in output voltage when subjected to -65°F operation.

## 1. INTRODUCTION

There has been for some time a need for a miniature, high-voltage battery to maintain charge on a capacitor. To satisfy this need, the battery described herein (figure 1) was developed with the major efforts being directed toward (1) a stable electrochemical system, (2) adequate cell-to-cell sealing, and (3) low-temperature operation. A stable electrochemical system is necessary because of the 0.005 to 0.008-in. plate separation that is needed for miniaturizing a high-voltage stack; also, the battery is made in the active condition and should have a shelf life greater than five years, with elevated temperature storage for several months. Adequate cell-to-cell sealing is important since even a slight amount of intercell leakage, electronic or electrolytic, will cause self-discharge of the small capacity (5 coulombs) in a short time. Low-temperature operation (-65°F) was a significant objective inasmuch as miniature high-voltage batteries seldom have this capability.

## 2. CELL CHEMISTRY

The electrochemical system consists of Zn/ZnCl<sub>2</sub>/Ag<sub>2</sub>S, Ag. The zinc chloride electrolyte is a 51-percent solution (the eutectic mixture) and freezes at -77°F. The electrolyte is saturated with zinc oxide, bringing the pH to about 10, which virtually eliminates the corrosion at the zinc

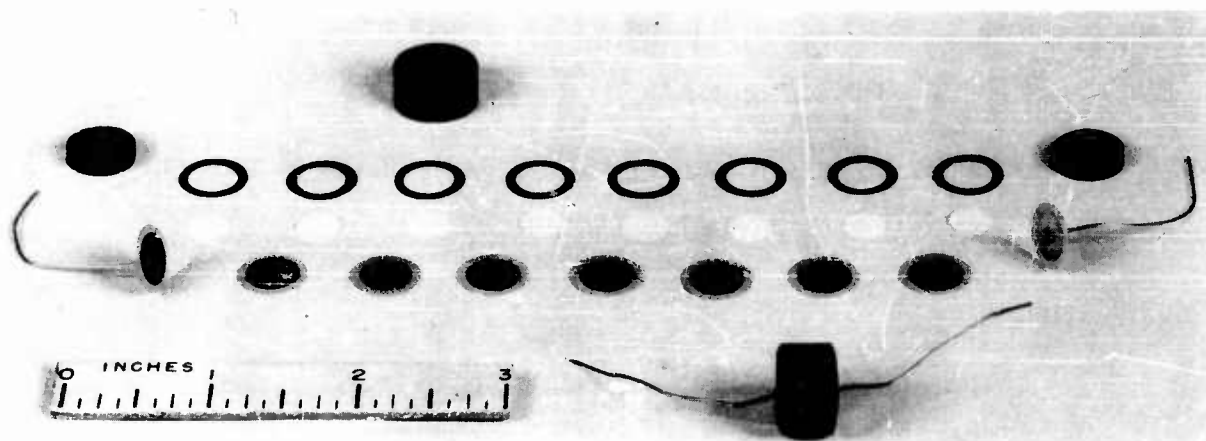


Figure 1. 6 v battery, disassembled

electrode. The positive electrode consists of a very thin silver sponge (on sheet silver) that is partially converted to the sulfide. The insolubility of the sulfide results in a very stable electrode.

During discharge, the electrolyte composition remains constant. Zinc ions enter solution at the negative electrode and silver sulfide is reduced to silver at the positive electrode. As soon as the sulfide ion is free, it combines with a zinc ion from solution. This process controls the sulfide ion concentration, which in turn controls the silver ion concentration to maintain the emf of the cell at a constant value of about 0.78 v. The product, insoluble zinc sulfide, forms on the silver rather than on the zinc electrode.

The overall cell reaction is:



At the negative electrode:  $\text{Zn} \longrightarrow \text{Zn}^{++} + 2 e$

At the positive electrode:  $\text{Ag}_2\text{S} + 2 e \longrightarrow 2 \text{Ag} + \text{S}^{=}$

Then:  $\text{Zn}^{++} + \text{S}^{=} \longrightarrow \text{ZnS}$

This last reaction controls the sulfide ion concentration according to the solubility product:

$$K_{\text{sol}} \text{ZnS} = [\text{Zn}^{++}] [\text{S}^{=}] = 1.2 \times 10^{-23}$$

Since  $[\text{Zn}^{++}] = 8.0 \text{ molar}$

$$[\text{S}^{=}] = \frac{1.2 \times 10^{-23}}{8.0} = 1.5 \times 10^{-24}$$

The sulfide ion concentration in turn controls the silver ion concentration as follows:

$$K_{\text{sol}} \text{Ag}_2\text{S} = [\text{Ag}^+]^2 [\text{S}^{=}] = 1.6 \times 10^{-49}$$

$$[\text{Ag}^+]^2 = \frac{1.6 \times 10^{-49}}{1.5 \times 10^{-24}} = 1.1 \times 10^{-25}$$

$$[\text{Ag}^+] = 3.3 \times 10^{-13}$$

The emf of the half cell,  $\text{Ag}^+ \longrightarrow \text{Ag}$ , can then be determined by the Nernst equation:

$$\begin{aligned} E &= E_0 - 0.059 \log [\text{Ag}^+] \\ &= -0.7996 - 0.059 \log (3.3 \times 10^{-13}) \\ &= -0.0632 \text{ volt} \end{aligned}$$

And the emf at the negative electrode ( $\text{Zn} \longrightarrow \text{Zn}^{++}$ ):

$$\begin{aligned} E &= E_0 - \frac{0.059}{2} \log [\text{Zn}^{++}] \\ &= +0.7628 - \frac{0.059}{2} \log (8.0) \\ &= +0.7362 \text{ volt} \end{aligned}$$

Total cell emf =  $0.7362 - (-0.0632) = 0.7994 \text{ volt}$ . This value is in reasonable agreement with the experimental value of  $0.775 \text{ v/cell}$  (section 4). The above calculations apply at  $+25^\circ\text{C}$ .

This control of the  $\text{S}^{=}$  and  $\text{Ag}^+$  ion concentrations along with a constant electrolyte composition, causes the OCV (open-circuit voltage)

to be constant for various states of discharge.

### 3. CELL STACKING AND SEALING

Teflon and epoxy resin are used for hermetically sealing the individual cells. Figure 2 shows the arrangement of these materials. Teflon has an electrical resistivity of  $10^{15}$  ohm-cm, and is flexible to  $-65^{\circ}\text{F}$ , which allows for the differential expansion between it and the metal plates. The outer border of the plates are first coated with a heat-curing epoxy-phenolic coating. This is applied to clean silver, the active cell materials being confined to the central area of the plates. Gaskets are punched from 0.009-in. sheet Teflon. These are given a sodium-naphthalene-tetrahydrofuran treatment to make them bondable to epoxy. Just prior to stacking, a thin film of epoxy-Thiokol is applied to both sides of the gaskets. The epoxy cures at room temperature after stacking, thus cementing the stack into a single unit. The following procedures are therefore necessary in stacking:

- (1) The silver plate with active materials and prime-coated border;
- (2) Filter paper separator almost saturated with electrolyte;  
and
- (3) Teflon gasket with a thin film of epoxy on both sides.

The epoxy-Thiokol and epoxy-phenolic coatings are flexible for temperature cycling. The surface resistivity of the surface-treated Teflon is about  $10^{13}$  ohms and maximum water vapor absorption 0.005 percent.

### 4. EXPERIMENTAL DETAILS

#### 4.1 Electrolyte and Positive-Plate Materials

In establishing this electrochemical system, several different electrolytes and positive-plate materials were examined. Silver chloride and silver bromide were found to form complexes  $\text{AgCl}_2^-$  and  $\text{AgBr}_2^-$ , which were somewhat soluble in the electrolyte. Single cells using these materials showed poor shelf life in that the complexes were reduced at the anode, causing treeing which soon shorts out the cell. Silver iodide was a little better in this respect, but the voltage varied with the state of discharge and was lower than desired.



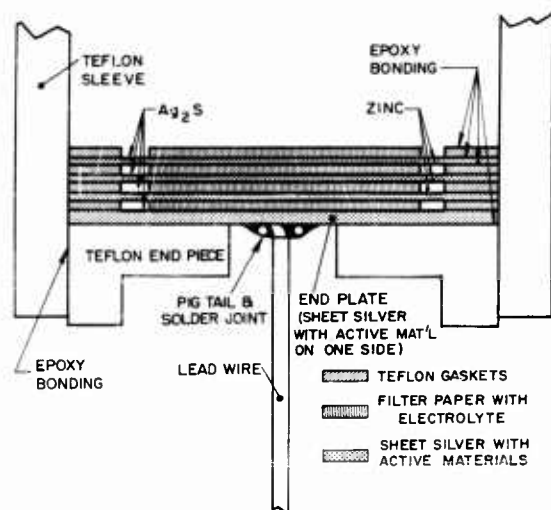


Figure 2. Stacking and sealing arrangement of cells (cross-section)

Regarding the electrolyte, there are only a few inorganic materials that will form eutectic solutions freezing below  $-65^\circ\text{F}$ . A neutral salt was chosen for long shelf life with the zinc electrode. Calcium chloride saturated with calcium oxide was tried; although the cell voltage was good, it varied with the state of discharge and gave poor recovery time after surges.

In trying these various systems, silver sulfide electrode showed the best storage, and the use of zinc chloride along with it provided for the most stable potential during discharge.

Figure 3 shows the discharge of an early designed single test cell. The capacity obtained was greater

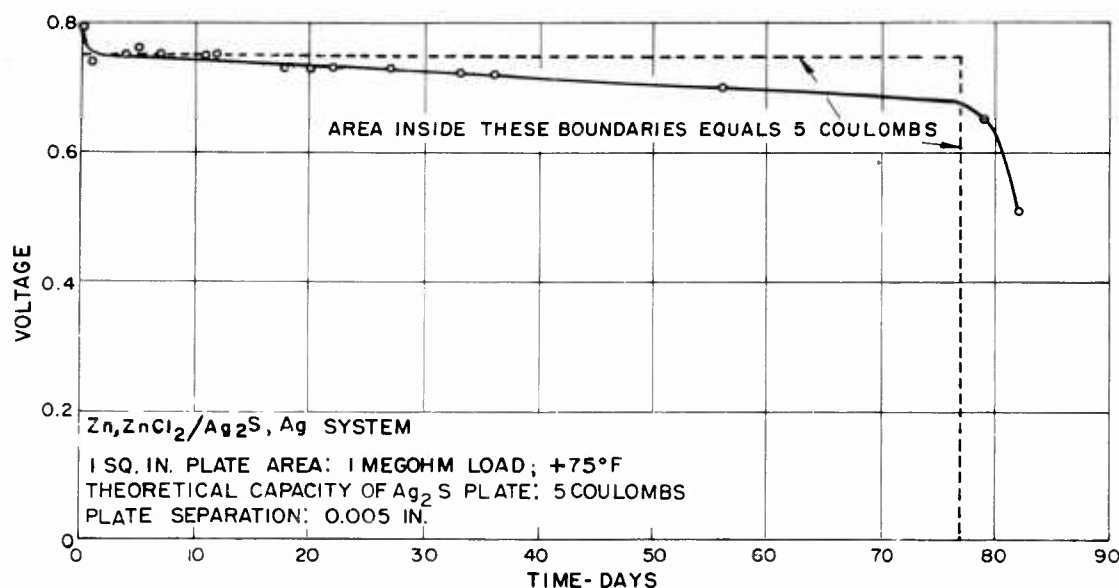


Figure 3. Discharge of experimental single cell,  $+75^\circ\text{F}$

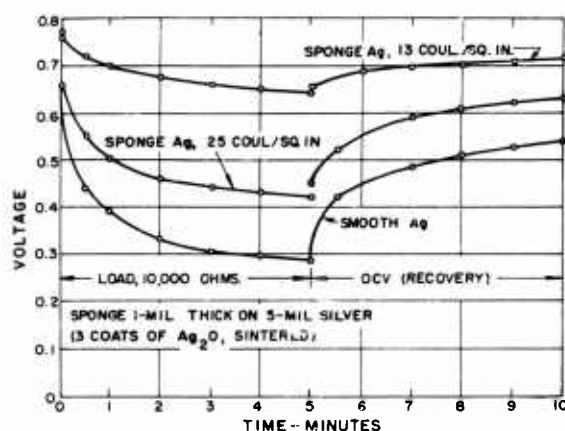


Figure 4. Discharge of single cells at  $-40^{\circ}\text{F}$ , plate area = 2 sq. in.

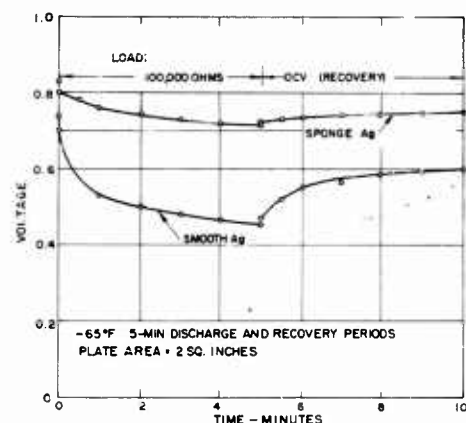


Figure 5. Discharges of single cells

Figure 5 shows the  $-65^{\circ}\text{F}$  performance of cells with silver sulfide on sponge and on smooth silver.

#### 4.2 Zinc Stability

Experiments were performed to determine various means of reducing gassing at the zinc electrode. Strips of zinc 1 in. x 10 in. x 0.001 in. were coiled and placed in separate beakers of electrolyte (51 percent  $\text{ZnCl}_2$ ).

than 95 percent of the theoretical capacity. The cell consisted of sheet zinc, filter paper impregnated with 51 percent zinc chloride, and sheet silver whose surface was electrolytically oxidized to silver sulfide (5 coulombs). The cell was held between two heavy sheets of lucite that were bolted at the corners, exposing a plate area of 1 sq in.

Figure 4 shows a major low-temperature improvement that resulted when a sponge surface--rather than a smooth surface--was used on the silver electrode. The procedure consisted in painting on a silver oxide water paste and heating to  $1000^{\circ}\text{F}$  for 10 min, which reduced the silver and sintered the surface. The process was repeated until a 0.002-in. sponge layer was built up. The sponge was partially oxidized to silver sulfide. Curve B shows that if too much of the sponge is converted to silver sulfide, the performance drops due to the smaller amount of silver exposed to the electrolyte. Curve C shows performance with a very little silver exposed.

An inverted funnel and calibrated test tube, initially full of electrolyte, were placed over each specimen to collect the generated gas. Different materials were added to inhibit gassing as follows:

Beaker No. 1 - 0.07 percent  $\text{Hg Cl}_2$

Beaker No. 2 - 1.0 percent Dichromate

Beaker No. 3 - 2.0 percent Borax

Beaker No. 4 - Saturated with  $\text{ZnO}$

Beaker No. 5 - Control

The beakers were placed in the oven at  $+ 165^\circ\text{F}$  and observed periodically. As can be seen in figure 6, zinc oxide gave the best results. Probably a combination of this treatment with one of the others would give a further improvement.

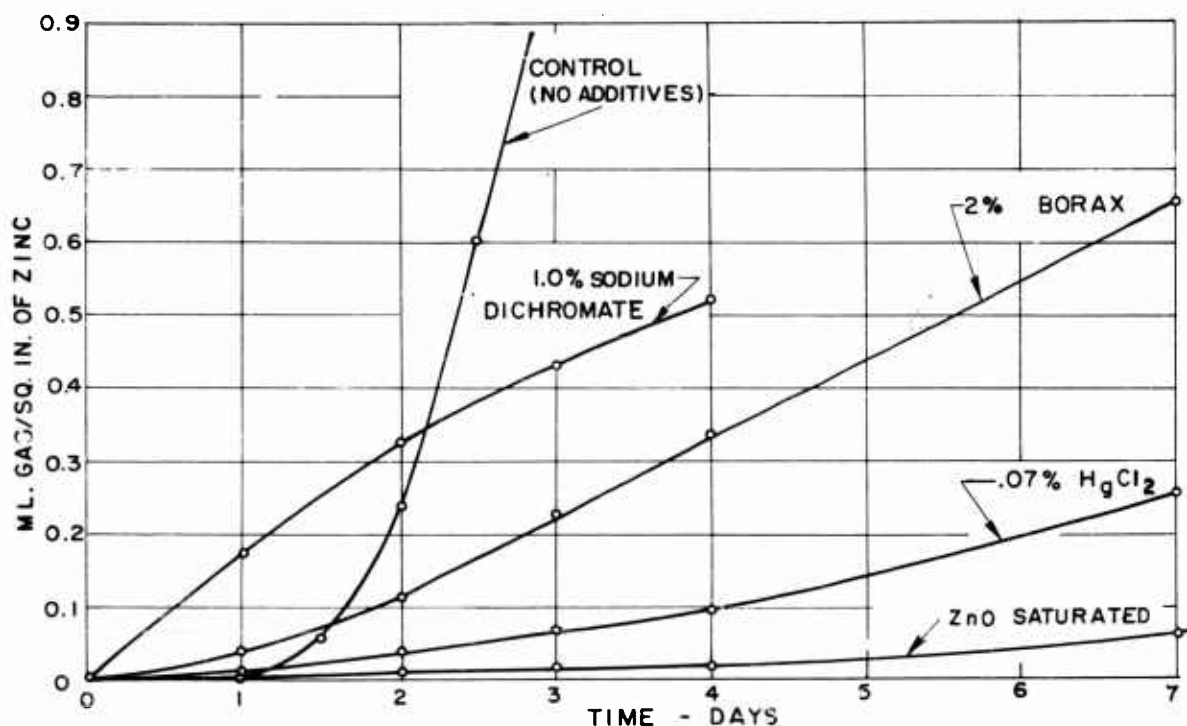


Figure 6. Rate of hydrogen evolution on zinc with modified electrolytes

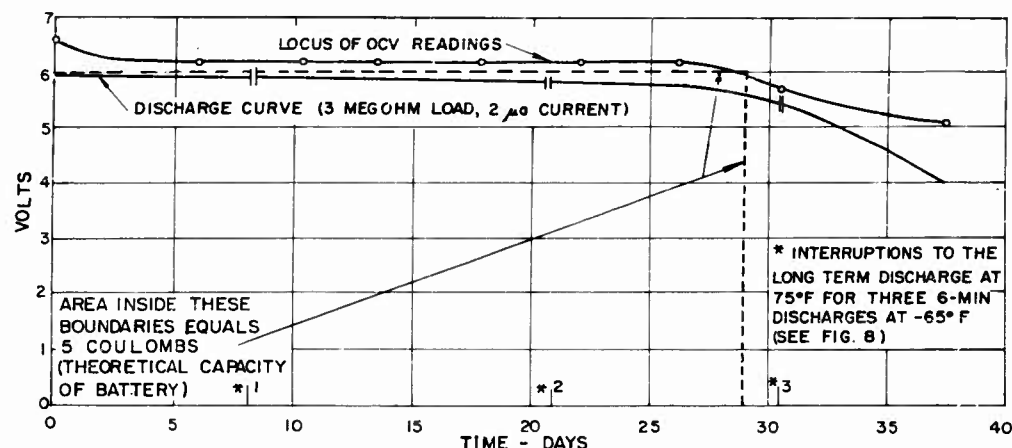


Figure 7. Battery #1, room temperature discharge

## 5. BATTERY PERFORMANCE

Figure 7 shows the room temperature discharge curve of a completed 8-cell, 6-v battery (No. 1); the effects of opening the circuit periodically to check the OCV at various stages of discharge are indicated by the upper curve. The asterisks indicate points where the battery was lowered to  $-65^{\circ}\text{F}$  and given 6-min discharge tests. These low-temperature test results are shown in figure 8. It is shown here that the battery's low-temperature performance is essentially as good at the end of the discharge life as it is at the beginning.

Figures 9 and 10 show the elevated temperature storage life of a similar unit (No. 2). This battery was stored at  $+125^{\circ}\text{F}$  and periodically given a  $-65^{\circ}\text{F}$  and  $-40^{\circ}\text{F}$  6-min discharge. These tests showed that the battery will function satisfactorily at  $-65^{\circ}\text{F}$  after a month of storage at the high temperature.

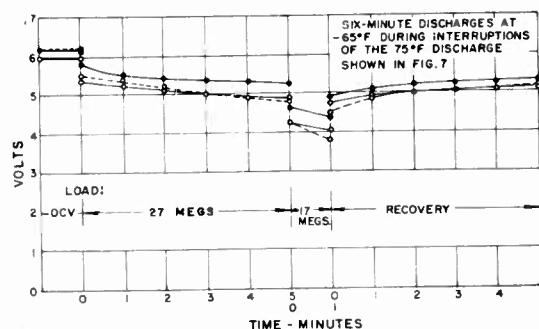


Figure 8. Battery #1,  $-65^{\circ}\text{F}$

## 6. RECOMMENDATIONS FOR FUTURE WORK

This system should be applicable and therefore considered wherever a high-voltage low-drain battery is needed. The number of units tested

however, is insufficient to determine manufacturing and applications problems. Further fabrication and testing of batteries should be undertaken to reveal any such problems.

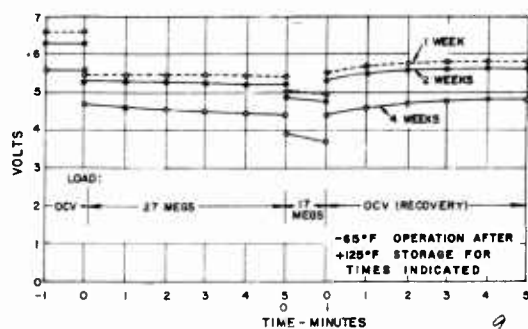


Figure 9. Battery #2, storage tests

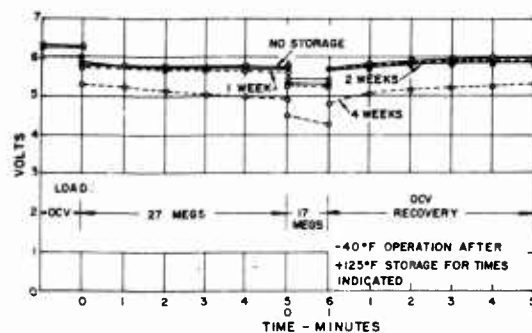


Figure 10. Battery #2, storage tests

UNCLASSIFIED

UNCLASSIFIED